THE UNIVERSITY OF CALGARY

Dust Features in Carbon-rich Planetary Nebulae

by

Albertina Hsien-Jean Pei

A THESIS

SUBMITTED TO THE FACULTY OF GRADUATE STUDIES

IN PARTIAL FULFILLMENT OF THE REQUIREMENTS FOR THE

DEGREE OF MASTER OF SCIENCE

DEPARTMENT OF PHYSICS AND ASTRONOMY

CALGARY, ALBERTA

APRIL, 2002

THE UNIVERSITY OF CALGARY

FACULTY OF GRADUATE STUDIES

The undersigned certify that they have read, and recommend to the Faculty of Graduate Studies for acceptance, a thesis entitled "Dust Features in Carbon-rich Planetary Nebulae" submitted by Albertina Hsien-Jean Pei in partial fulfillment of the requirements for the degree of Master of Science.

Kevin Volk

Chairman, Dr. Kevin Volk
Department of Physics and Astronomy

Dr. Sun Kwok
Department of Physics and Astronomy

Dr. A. R. Taylor
Department of Physics and Astronomy

Dr. Thomas W. Swaddle
Department of Chemistry

10 APRIL 2002

Date

Abstract

In this thesis, we present computer models of two carbon-rich planetary nebulae, IC 418 and NGC 7027, which explore the presence and strength of dust features, particularly those observed at 21, 27 and 33 μm. This study is based on recent work which derived the feature profiles from observations of proto-planetary nebula.

Models were constructed using a combination of output from computer programs Cloudy by G. Ferland and DUSTCD based on work by C. Leung to reproduce spherically-symmetric approximations of the objects. The models were successful in simulating the spectrum from the two objects as compared to detailed infrared observations from the Infrared Space Observatory, and observed $H\beta$ flux, selected optical line ratios and the stellar V magnitude.

The strengths of the features at 27 and 33 μm are found to be consistent with what is seen at the proto-planetary nebula stage. The strengths are on the weaker end of those found in PPNe but it is unclear if this is an evolution from the original strengths or those inherent to these objects for other reasons. The 21 μm feature modeled in IC 418, in particular, is weak but is one of the first detections in PNe of the feature.

Both objects studied are young PN less than 1000 years into the PN phase. It will be important to continue studies of well-observed objects both closer to the transition from PPN to PN and from PN to older objects in order to understand the evolution of the dust and these three dust features.

Table of Contents

List of Tables

List of Figures

Chapter 1

Introduction

Planetary nebulae (PNe) were first observed in the late 1700s by Charles Messier, a French astronomer searching for comets. He categorized these objects as "nebulae" which is Latin for "clouds". When William Herschel took higher resolution observations of these objects, he could only resolve some into individual stars. Of the ones that could not be resolved, the name "planetary nebulae" was given to the set of objects that were green in colour and round in appearance.

In the mid-1800s, the spectroscope was introduced to observational astronomy. Observations of stars had revealed continuous spectra. Planetary nebulae (PNe), however, surprised astronomers by revealing instead a single strong emission line. Higher resolution spectra revealed a group of three lines. One was identified as the $H\alpha$ Balmer line, while the other two lines had never before been observed and were dubbed "nebulium" lines. In 1927, the lines would be identified as lines emitted from doubly-ionized oxygen (hereafter, [OIII]; See Section A.1). This line is today considered to be a primary identification line for PN. With the presence of both [OIII] and $H\alpha$, it became clear that PNe are fuelled by higher temperature central sources than expected. Since [OIII] lines are collisionally excited, the gas density in the region must dense enough to fill the upper levels but low enough for spontaneous decay processes to dominate.

In the years since, PNe have been identified as being transition objects between Asymptotic Giant Branch (AGB) stars and white dwarf (WD) stars. Observations plotted on the Hertsprung-Russell diagram (HRD) show that these objects fill the gap between the AGB branch and the cluster of WD stars in the lower left region. (See Figure 1.1.) The HRD is a log-log plot of stellar temperature versus stellar luminosity. Originally, stars were predicted to be scattered throughout such a plot. It turns out that stars follow specific tracks as they evolve. The diagram shown below depicts the evolutionary tracks of intermediate mass stars that become PN.

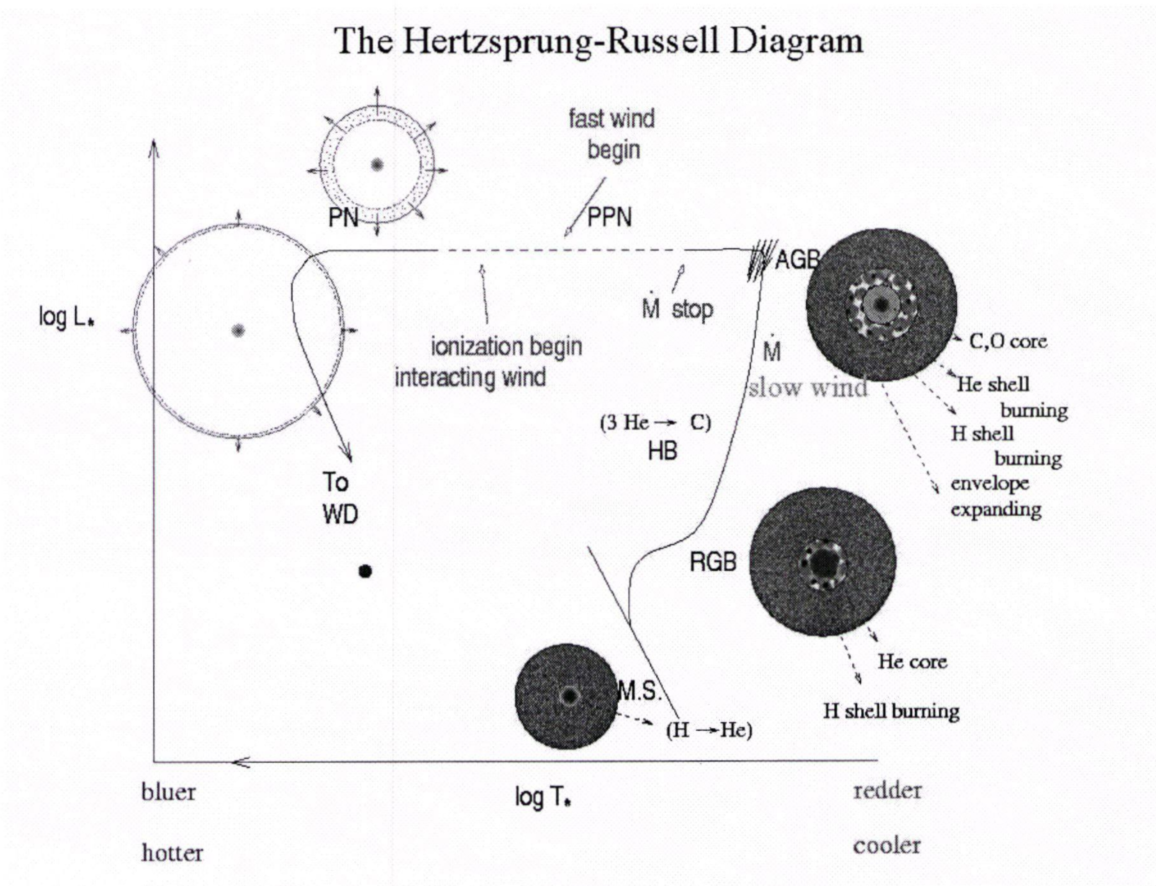

Figure 1.1: HR Diagram for stellar evolution relevant for PN evolution. (From Su (2000).)

A star's energy production is due to nuclear reactions that fuse atomic nuclei together to produce heavier atoms. Stellar nuclear fusion occurs in two regions.

Core burning refers to nuclear reactions which fuse atoms in the core of a star, while *shell burning* refers to the fusion taking place in a shell of nuclear fuel surrounding the core. Depending on their mass and age, different fuels will burn in the core or in the shell. Stars spend the largest portion of their lives on the main sequence (MS) burning hydrogen in their cores. MS stars having a mass between 0.1 $M_\odot$ and 10 $M_\odot$ are large enough to ignite their cores past core-hydrogen burning to core-helium burning but are not large enough to ignite the carbon-oxygen core that results. These are the stars that will produce PN late in their evolution. Once all the nuclear fusion has ceased, these stars are destined to become cool carbon-oxygen cores that define the WD stage. Stars larger than $\sim$10 $M_\odot$ will continue a chain of nuclear fusion reactions in their cores creating heavier and heavier elements until solid iron is created in the core. A supernova explosion will mark the end of these high-mass stars.

The red giant (RG) phase is defined by a contracting helium core and the fusion of hydrogen in the shells of intermediate mass (0.1 $M_\odot \leq M_* \leq 10$ $M_\odot$) stars. After exhausting the helium fuel in the core in a "helium main sequence" following the RG phase, the star enters a turbulent phase of alternating periods of shell-hydrogen and shell-helium burning, thermal pulses and helium flashes. This is the AGB phase where a great deal of core material is churned up into the envelope. Throughout the giant phases, the central cores bear a striking resemblance to the central stars of planetary nebulae (CSPN) and the composition of their envelopes is much like that of the future nebula. Observations have shown the presence of molecules and dust in the envelope as the AGB evolves towards the PN phase.

Material is constantly being blown away from the surface of the star through wind processes similar to our solar wind but with varying strengths and densities. The interactions between the various morphologies of this wind result in a cluster of gas surrounding the star. The PN phase occurs if the core temperature becomes hot enough to ionize the surrounding mass of ejecta before it drifts too far away or dissipates into the interstellar medium (ISM). This bright, ionized region is what is observed to the delight of amateur and professional astronomers alike.

PNe serve as excellent storytellers for the life of their central stars. The various densities of matter and interactions and morphologies observed in the present day PN describe the stars' past. Each layer containing different compositions and abundances indicating the chemical state of the central star at various stages of its life; observed at different distances from the star, indicating when it was ejected. Each of these details helps to chronical the past 100,000 years of life of the central star.

1.1 Interacting Winds Model

The interacting stellar winds (ISW) model was proposed by Kwok, Purton and Fitzgerald (1978) to describe the formation and dynamics of planetary nebulae and continues to be the leading model. The model, which assumes a single central heating source, describes the interaction between the slow ($\sim$10 km/s), high density wind ($10^{-4} M_{\odot}$/year) of the precursor red giant phase and the fast ($\sim$1000-4000 km/s), low density wind ($10^{-7} M_{\odot}$/year) of the central star of the PN. The two winds collide, squeezing a portion of the early slow wind into a high density shell with a contact discontinuity at the interface. The fast wind produces two shock fronts: an inner shock moving towards the central star and an outward moving shock at the outer edge of the high density shell. The region in between the inner shock and the contact discontinuity contains the fast wind material which, having been reflected off the slow wind region, becomes trapped.

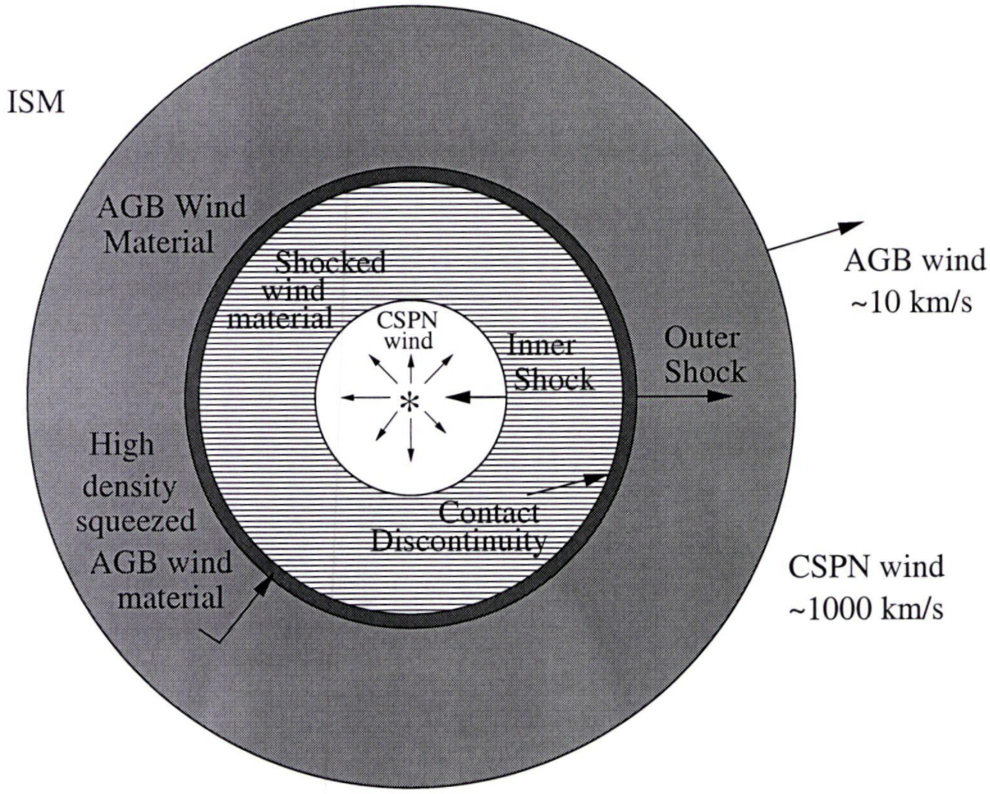

Figure 1.2: The Interacting Stellar Winds Model.

The basic model used has 3 key regions:

1. a low density hollow cavity

2. a constant high density, completely ionized region (modeled using Cloudy, See Chapter 3.2)

3. a neutral wind region (modeled using DUSTCD, See Chapter 3.3)

The ionized region is heated by the UV stellar continuum and the diffuse radiation field. The diffuse field is the radiation that is absorbed and re-emitted by the gas in the ionized region. The emerging radiation field from the ionized region of the nebula is composed of forbidden and recombination line emission and the free-free/bound-free (see Section 3.2.2) nebular continuum. The neutral wind region is assumed to be optically-thin to free-free continuum and is thus heated by the remaining nebular continuum and line emissions.

In young PNe, the ionized region is expected to be ionization bounded, meaning all the ionizing photons emitted by the central star are absorbed by the nebula.

1.2 The Infrared Excess

Despite the presence of dust in the preceding AGB phase, it was believed that the same would not be true for PN since the electron plasma of the ionized region should effectively destroy any grains surrounding the central star that were not pushed out by radiation pressure from the stellar UV photons. The IR region was predicted to look similar to the optical range with a weak continuum and strong emission lines. So, it came as quite a surprise when a strong infrared excess was observed in PNe (Zhang & Kwok (1992), Barlow & Cohen (1974)).

Figure 1.3 shows observations of NGC 7027 (in blue, yellow and black) and a model of the nebula assuming no dust content (in green). While free-free (ff) radiation (see Section 3.2.2) dominates in the far IR in the model, the observed emissions in that range cannot be explained by the ff process alone. The continuum emission in the far IR, peaking near 30 μm has an equivalent blackbody temperature of 100 K.

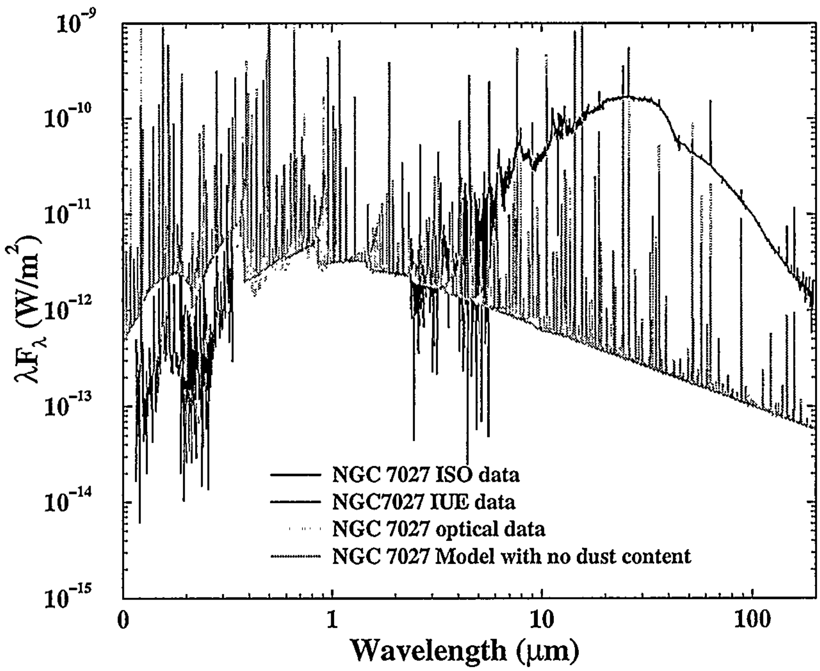

Figure 1.3: A model of NGC 7027 with no dust is shown in green and is compared to the observations of the PN. The model represents the spectrum and emissions that were expected: a weak continuum and strong lines. The observed excess in the infrared is significant.

Therefore, unlike typical PN plasma temperatures of 10^4 K, the material responsible for the IR excess will be a relatively cool component of PNe but warmer than ISM material, which has a temperature around 30 K. The broadness of the continuum would also suggest it is not of atomic or molecular origin, which produces lines or much narrower features. The best explanation for these observations would be the presence of larger particles such as dust associated with the PN.

1.3 PN Circumstellar Chemistry

PNe are found to be either carbon-rich or oxygen-rich. The dust content is expected to be different in these two cases as a result of the different chemical and molecular content of the precursor star and the early PN environment. In carbon-rich PN, more carbon-based dust (amorphous carbon, graphite) is observed, whereas oxygen-rich PN show predominantly silicate-type dust grains. (See Section 1.6.1).

Recall that AGB stars are not sufficiently massive to ignite their cores past He-core burning and indeed, they die off as small cooling, compact carbon-oxygen stars (WD). The ashes at the core of stars are brought to the surface and ejected into the circumstellar shell by "dredge-up" processes, where convection churns up material from deep within the star. The complicated process of dredge-up is not well understood, although it is seen throughout post-MS evolution. It is sufficient to recognize that the outer envelope of these late-stage stars will be a complex atomic mix heavy with C and O.

There is likely some degree of mass-dependence on the C-rich and O-rich phenomenon. For C-rich stars, there needs to be adequate carbon brought to the surface to overpower the original oxygen in the atmosphere. Stars that are on the low-mass end of the PN precursor scale are likely unable to churn up enough carbon into the atmosphere, while larger mass precursor objects have too much oxygen in the atmosphere to overpower. It appears that the carbon-rich PNe represent an intermediate range of precursor star masses.

In any case, the free oxygen and carbon atoms will first combine to form CO molecules (see Section 1.4). In a C-rich environment, the remaining atoms will be carbon which will combine with other circumstellar material to form various carbon-based dust grains and molecules (eg. HCN, HNC, HC_3N, CS, nano-diamonds, amorphous carbon, graphite. See Section 1.6.1.). In O-rich environments, all the free carbon will combine to again form CO molecules, allowing the remaining material to form oxygen-based grains (eg. SiO, SO, amorphous and crystalline silicates. See Section 1.6.1.). Maser emission from OH, H_2O and SiO are also indicators of O-rich environments (Bujarrabal *et al.* 1994).

1.4 Molecular Component of PN

Longer wavelength emissions give insight into the molecular gas in PNe. Compared to atomic transitions, molecular transitions are largely due to rotational and vibrational transitions resulting from the presence of more than one nucleus. These transitions have a much smaller energy difference than atomic transitions and produce a wider range of emission lines in the IR and radio ranges.

The most abundant molecule is molecular hydrogen but it is difficult to detect. H_2 has identical nuclei in a symmetric configuration and does not have a permanent electric or magnetic dipole moment. As a result, transitions are limited to those due to electric quadrupole moments and are difficult to detect. The 2.121 μm vibrational line in particular is excited by either shocked gas or fluorescent emission and is observed as a means to map the structure and dynamics of PN.

Aside from H_2, the CO molecule is the most abundant molecule in the ISM. In the PN environment rich in H, C, N and O, the CO molecule is favoured over other molecular combinations. CO is also readily excitable by collisions and emits many lines throughout the millimeter and submillimetre range.

The structure of the molecular envelope can be mapped through the analysis of the various CO emission lines. Each line will have different density, temperature and abundance dependencies. Therefore, the presence and strength of the various emission lines at different locations in the nebula serve as a means to map the structure of the nebula. Blue-shifting and red-shifting of the line emissions will also indicate a direction and velocity of the nebular expansion.

This type of observation was done by Jaminet *et al.* (1991) to map the structure of NGC 7027 and show, among other things, fast and asymmetric outflows of material surrounding the nebula. (See Chapter 5.)

1.5 Dust

The existence of dust in PNe has largely been accepted following the observations of large infrared excess that could not be explained by the nebular continuum alone. The Infrared Astronomical Satellite (IRAS) and the Infrared Space Observatory (ISO, see Section 2.1.1) would provide a new level of clarity in the infrared to improve studies of the dust and molecular component of PNe. By tracing the dust from the AGB phase through to the PN phase, a better understanding of late-stage stellar evolution and the outflow of material into the ISM can be developed.

The dust component is a complex system having both a warm and a cool component (Kwok 1980). The warm component is believed to be located within the ionized region while the cool dust is contained in a neutral region outside. Observations show a wider underlying continuum peaking in the IR and several sharper features throughout the spectrum. Different grains are responsible for different features with several key types being presented in Section 1.6.1.

Recent work by Volk *et al.* (2002) studied the profiles of emission features observed in proto-planetary nebulae (PPN) at 21, 27 and 33 μm. The extracted features will be added to models for IC 418 as described in Chapter 4 and as described for NGC 7027 in Chapter 5. We want to see how these features fit into the PN dust component and seek some insight into what the evolution of the features might be. In the next section, we introduce various dust grains and the previous work of Volk *et al.* (2002) which is the basis of the work done here.

1.6 Dust Features

The dust features are signature emission curves that have been found in many stellar and ISM sources. It is not clear what the carrier particles are for all the features but many studies have been undertaken suggesting various possibilities. The carriers themselves are not the focus of this study but instead the presence and strengths of the features in the PN stage are investigated. This will form one part of the puzzle in describing and explaining the properties of the surrounding dust during the evolution of the central source objects in this critical stellar evolutionary phase.

Previous lower resolution observations show a single, wide feature peaking at 30 μm in C-rich objects which has often been attributed to MgS (Goebel *et al.* 1985). The more recent ISO data and the work of Volk *et al.* (2002) has distinguished two separate features: one peaking at 27 μm and one at 33 μm. These two features appear together in all PPNe observations, which suggests that the carrier particles for both are related. A third feature of significance is the 21 μm feature. This feature is most likely due to a carbon-based carrier since it is only seen in C-rich objects. The broadness of the feature suggests that it is a molecular mode as opposed to an atomic mode. Molecules have many more modes available as a result of various rotational and vibrational modes. This results in a broader range of emission lines and thus a broader feature. Atoms have limited transitions available and will have sharper emission features. The 21 μm feature is always accompanied by the 27 and 33 μm features although the strength does not appear correlated to the two.

There appears to be a definite evolution to the presence and strengths of the features from the stellar AGB phase through the PPN phase to PNe (Figure 1.4). This evolution will describe changes to the properties of the carrier particles themselves and with respect to the surrounding nebular environment. In particular, the 21 μm feature is very weak in the AGB phase, but much stronger in PPNe, which suggests the carriers develop during the transition period.

In order to isolate the dust features, the portion of the continuum which is not due to the features (the base continuum or underlying continuum) must be removed from the observed data. This task is less complicated at the PPN stage since it is assumed that the only radiation field heating the dust is from the central star providing a simpler radiation transfer model. Volk *et al.* (2002) have looked at a number of proto-planetary nebulae (PPNe) in order to derive the shapes of the 21, 27 and 33 μm features. Figure 1.5 shows the underlying amorphous carbon continuum compared to the overall ISO spectrum for IRAS 19500−1709.

Once the base continuum is removed, a fitting procedure is applied to determine the emission profiles of each feature. When normalized, the features from the sources

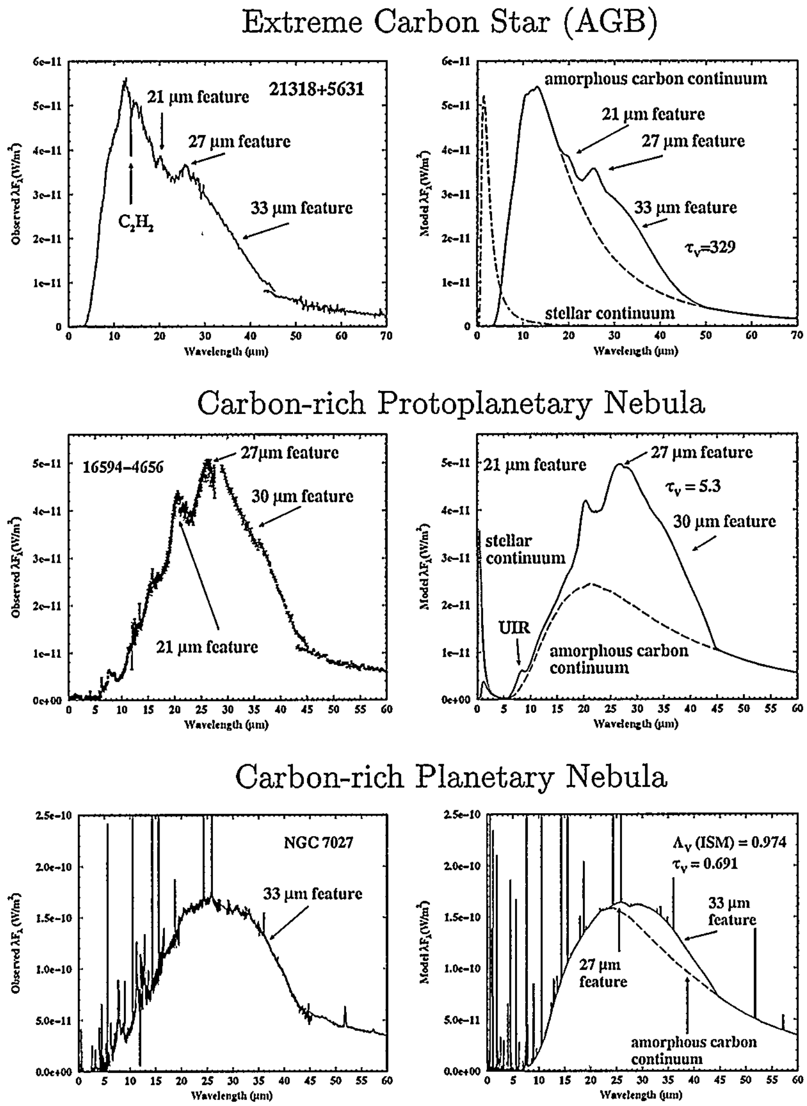

Figure 1.4: These images show the difference in feature strengths from the Extreme Carbon Star stage to Protoplanetary Nebulae to the PN stage. (From Volk *et al.* 2002)

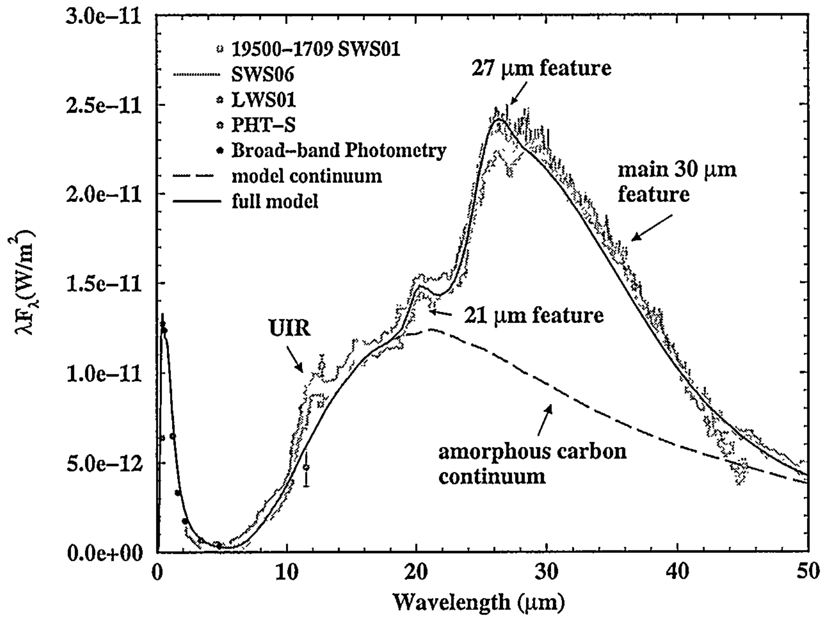

Figure 1.5: A best-fit model is overlayed on the ISO spectra from IRAS 19500−1709 (Volk 2001). The underlying dust spectrum is shown with a dashed line. The three IR features are also noted.

studied were found to be similar and thus are taken to be a good representation of the true feature. An example is shown in Figure 1.6 for IRAS 19500−1709.

The derived features at 21, 27 and 33 μm will be added to theoretical PN models and compared to ISO data in order to get insight into their presence at this evolutionary stage.

We will first need to establish the underlying continuum of the dust before applying the features. The secondary interest will be to confirm the presence of some of the other emission features that are clear in the ISO observations.

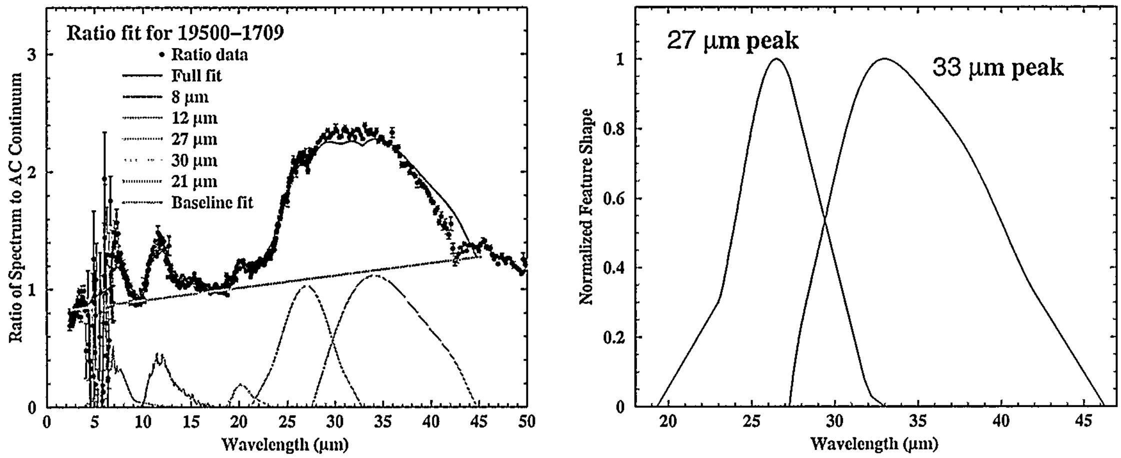

Figure 1.6: 19500−1709 fit with the features shown on the left. The derived shapes of the 27 and 33 μm features are on the right. (Volk *et al.* 2002)

1.6.1 Grain Types

Much like the method used to derive the shapes of the various features, the PN models consider the inclusion of grains in two ways. There is the underlying dust continuum which tends to be a wider, flatter curve and a set of dust features which have sharper peaks.

The underlying continuum is more consistent with an amorphous grain, as opposed to anything crystalline in nature. Crystalline structures have ordered lattices with the constituent atoms in specific repeated patterns. The symmetry of the lattice limits the system to certain vibrational modes and will result in sharp feature emissions. The amorphous structure is a loose, random, asymmetric cluster of atoms. This type of system has a wider range of vibrational modes due to the range of bond angles and lengths not present in the more ordered crystalline structure. As a result, amorphous grains will give rise to a broader continuum (see Figure 1.5).

The ordered structure also requires slow cooling during formation to allow the atoms to settle into place in a crystal lattice. Since the AGB environment is a turbulent environment with grain temperatures dropping very quickly, it is more favourable to amorphous grain types which have their random structure "frozen" into place. It therefore comes as more of a surprise that features consistent with small amounts of crystalline solids have been discovered in PN spectra. However, the amorphous grain is the more abundant form of dust in PNe.

The main types of grains will be discussed here although not all of the grains were actually used in the models.

Graphite

Graphite describes carbon atoms in a hexagonal crystal structure, the most common configuration of crystalline carbon. Hoare (1990) compared model graphite grains to PN observations and found they were not a good fit to the underlying continuum. He showed that the amorphous carbon grain was the more likely carbon grain in carbon-rich PN.

Amorphous Carbon

Amorphous carbon (AmC) refers to loosely clustered carbon grains. The models presented here use an AmC grain model by Rouleau and Martin (1991) to produce the underlying dust continuum on top of which the dust features will be added.

The continuum produced by amorphous carbon (see Figure 1.5) is a product of a standard blackbody curve and the extinction efficiency (Q_λ) values calculated from the Mie Theory (see Section 3.1.1). These values adjust for the deviation of the continuum from the blackbody curve.

Silicate Grains

Silicate grains are believed to be the predominant grain in oxygen-rich PN environments having a $Mg_xFe_ySiO_z$ configuration with Mg and Fe sometimes being substituted by other heavy elements such as Co, Mn and Zn. Common forms include the olivines ($y = 2k$, $x = 2 - 2k$, $z = 4$ and $0 \leq k \leq 1$) and pyroxenes ($x = 1 - y$, $z = 3$ and $0 \leq y \leq 1$). Jäger *et al.* (1998) suggest that the magnesium-rich silicates ($k \sim 1$ for olivines or $y \sim 1$ for pyroxenes) are the most likely carriers of the observed silicate features. These grains can also be divided into amorphous and crystalline type grains, with the amorphous grains again being the predominant form having two main peaks at 10 and 18 μm. The crystalline silicates were expected to be rare but have recently been observed.

Silicon Carbide

SiC is another grain which has been observed in many objects. It is one of the first grains expected to form in carbon stars since it can form at temperatures above 2800K (Frenklach, Carmer & Feigelson (1989)). The typical SiC grain has two main configurations: the α-type has a hexagonal or rhombohedral structure and the β-type has a cubic structure. The grain has a signature peak at 11.3 μm with a width of 1.6 μm. An example is shown below in Figure 1.8.

The SiC feature shape in Figure 1.8 was extracted using a method similar to the PPN discussion in Section 1.6. The data region containing the feature is removed from the observations and a curve fitting routine is applied to the remaining data. The resultant best-fit curve is divided out from the complete set of observational data to isolate the feature profile. The feature is distinctly symmetric and fairly narrow

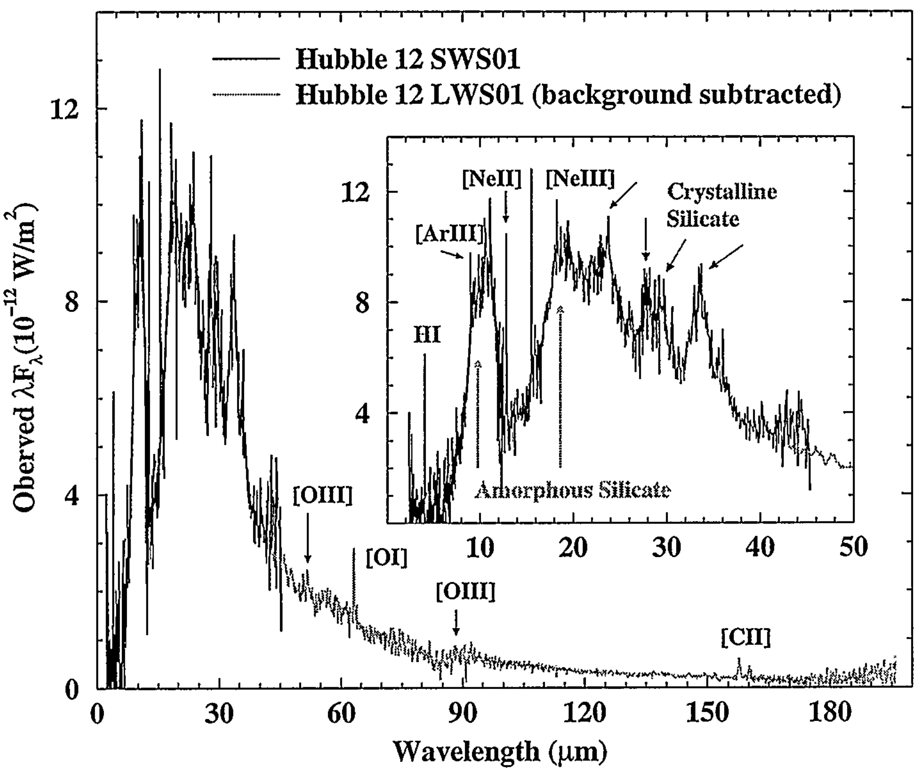

Figure 1.7: The amorphous and crystalline silicate features observed in HB12 are indicated in the inset image. (Volk 2001)

with a full width half maximum (FWHM) of 1.6 μm. This type of SiC feature is referred to as a "clean" or pure SiC feature, with the theoretical optical properties calculated directly from the Mie Theory (see Section 3.1.1).

It has also been suggested by Hoare (1990) citing Borghesi *et al.* (1985) that a "dirty" SiC grain would improve the fit and be more suitable compared to the SiC found in the ISM. The black or "dirty" SiC grains have been contaminated by other material, often being mixed or coated with amorphous-type carbon grains and give rise to a wider feature peaking at slightly longer wavelengths and having an extended tail on the long wavelength side.

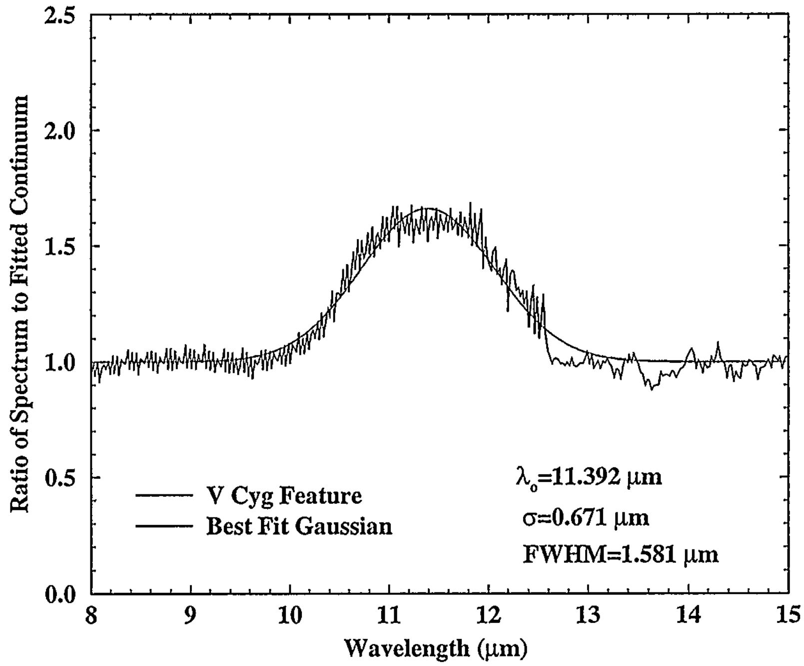

Figure 1.8: The SiC featured observed in V Cyg with a Gaussian fit. (Volk 2001)

Polycyclic Aromatic Hydrocarbons

Certain signature emission curves have already been determined for features peaking at 3.3, 6.2, 7.7, 8.7, 11.3 and 12.7 μm. This series, attributed to bending and stretching modes of C-C and C-H bonds, are collectively called polycyclic aromatic hydrocarbon (PAH) features. PAHs are basically clusters of benzene rings. Schutte *et al.* (1993) present a study on the relationship between the various peaks in this series of features. They show that there are various sensitivities to parameters including radial distribution and temperature that change the combined shape of the PAH emissions. It is sufficient for this study to confirm that the peaks are related to the PAH grains without being able to match all the feature strengths simultaneously.

Cloudy uses work by Schutte *et al.* (1993) and Bregman *et al.* (1989) to describe the PAH grains.

Chapter 2

Observational Background

In this chapter, we introduce the observational data that define our PN models, both as input values and as goodness-of-fit parameters. In order to create a model, we must have the basic information about the PNe including characteristics of the central star which fuels the system and the distance to the nebula. Sections 2.5 and 2.6 will discuss the methods used to determine them.

The primary goal of the models is to provide an overall fit to the spectrum observed by the Infrared Space Observatory (ISO). The ISO observations of PN spectra alone will not be sufficient to determine a reasonable fit for our models. Any number of PN geometries and dust content can produce similar results. Additional constraints from the physical processes which define PN systems need to be introduced as a means to fit the models. $H\beta$ flux and 5 GHz flux density are key observations which will serve as the main constraints to our models. The concepts of flux, magnitudes and luminosities will be discussed in Section 2.2.

As a check of the model results, the temperatures of the central star and the electron plasma as well as the electron density will be derived and compared to observations. Discussions of the electron temperatures and densities will be in Section 2.7.2 and 2.7.3 respectively.

2.1 Observational Data

The models are compared to data collected in the optical, in the ultraviolet (UV) by the International Ultraviolet Explorer (IUE), and in the infrared from both short wavelength and long wavelength spectrometer data from ISO. The primary concern will be with the infrared region but an overall spectral match is attempted with optical and IUE data where available. There does not appear to be a unique dust model to fit the observations, so we have used further constraints on the model with flux values and line ratio data for each PN.

2.1.1 Infrared Space Observatory

Infrared observations are important since a large range of vibrational and rotational transition modes of molecules and grains emit in this range and provide valuable information on abundances, densities and the overall structure of PN. Observations from the ground in the infrared are impeded because of the Earth's atmosphere, which absorbs most wavelengths in the mid- to far-infrared range. It is necessary to observe from space in order to collect useful data.

The ISO satellite, a project by the European Space Agency (ESA) carried four instruments including two spectrometers, the Short-wavelength Spectrometer (SWS) and the Long-wavelength spectrometer (LWS), providing unprecedented spectral resolution between 2.5 and 196.9 μm.

SWS observations span between 2.38 and 45.2 μm and are divided into two grating sections: SW (2.3-12.0 μm) and LW (11-45 μm). ISO has three different apertures and the SWS has four different 1x12 detector sets. Each of the twelve ISO bands uses a different combination of echelle order, aperture and detector set to collect the appropriate range of wavelength observations as shown in Table 2.1.

	Band	$\Delta\lambda$ (μm)	Order	Aperture No.	Aperture Area (″)	Detector	Sensitivity
SW	1A	2.38-2.60	SW4	1	14x20	InSb	0.6
	1B	2.60-3.02	SW3	1	14x20	InSb	0.6
	1D	3.02-3.52	SW3	2	14x20	InSb	1.1
	1E	3.52-4.08	SW2	2	14x20	InSb	1.1
	2A	4.08-5.30	SW2	2	14x20	Si:Ga	4.5
	2B	5.30-7.00	SW1	2	14x20	Si:Ga	4.5
	2C	7.00-12.00	SW1	3	14x20	Si:Ga	4.5
LW	3A	12.0-16.5	LW2	1	14x27	Si:As	6.5
	3C	16.5-19.5	LW2	2	14x27	Si:As	6.5
	3D	19.5-27.5	LW1	2	14x27	Si:As	6.5
	3E	27.5-29.0	LW1	3	20x27	Si:As	6.5
	4	29.0-45.2	LW1	3	20x33	Ge:Be	5.5

Table 2.1: SWS Observation Band Definitions. Taken from de Graauw (1998). The sensitivity is a ratio of in-orbit noise to ground noise.

The SWS01 observing mode scans the entire SWS wavelength range by sweeping light dispersed by a rotating mirror over the entire detector set. Each of twelve bands overlaps slightly with its neighbouring wavelength ranges to allow the best possible coverage when connected together.

LWS observations cover 43 to 196.9 μm between ten detectors, each detector related to a LWS band. The first five (SW) have ~10 μm-wide channels between 43 and 90 μm. The last five (LW) have ~20 μm-wide channels between 90 and 197 μm. The LWS01 observing mode is also a complete scan of the entire wavelength range of the instrument. Each LWS spectrum is composed of multiple scans across the single 1x10 detector.

The model spectra will be compared with the SWS01 and LWS01 observations of the PNe as the primary observational constraint.

2.2 Flux

Conceptually, intensity is the energy carried by a single ray from the source. Explicitly, intensity or brightness, I_ν, is the energy tranfer through a unit area (σ) per unit time (t) per unit frequency (ν) per unit solid angle (ω).

$$I_\nu = \frac{dE}{d\sigma \cos\theta d\omega dt d\nu} \tag{2.1}$$

where $\cos\theta$ is the angle between the normal to the area and the direction of the ray light. Intensity is typically expressed in units of erg cm^{-2} ster^{-1} s^{-1} Hz^{-1} = 10^{-3} W m^{-2} ster^{-1} Hz^{-1}.

Where intensity is energy for a single ray, *flux* is the energy carried by all rays passing through some area.

Flux density (or the monochromatic flux) is the energy carried through some unit area per unit time by photons of a specific frequency, ν,

$$F_\nu = \int I_\nu \cos\theta d\omega \tag{2.2}$$

$$= \frac{\int 4\pi j_\nu dV}{4\pi D^2} \tag{2.3}$$

where I_ν is the intensity of the photons, V is the volume and D is the distance to the object. $4\pi j_\nu$ is called the *total volume emissivity* and describes the energy emitted per unit time per unit volume. The total emissivities due to various different emission processes are described in Chapter 3.2.

The typical units in astronomy for flux density are erg cm^{-2} s^{-1} Hz^{-1} = 10^{-3} W m^{-2} Hz^{-1}. For radio astronomy, the Jansky is the standard unit which is 1 Jy = 10^{-26} W m^{-2} Hz^{-1}.

In general, any expression for energy emitted may be used and the radius of the observer's sphere can be defined in whichever manner fits.

Flux (or total flux) is integrated over all frequencies (or an integral over a finite range of frequencies for a spectral line) for a total energy

$$F = \int F_\nu d\nu. \tag{2.4}$$

In astronomy, the typical units of flux are erg cm^{-2} s^{-1}, while the SI unit is W/m^2.

2.2.1 $H\beta$ Flux

In a nebular environment that is optically thick to the Lyman continuum (see Appendix A.1.3) and lines, every Lyman photon is absorbed and each absorption will eventually result in a Balmer line photon. Since the Balmer line emission series has a weak, well-described temperature and density dependence, the total set of Balmer emissions can be calculated based on any single Balmer line for an assumed temperature and density. The most commonly observed line is the $H\beta$ line which is often used as a measure of the ionizing properties of the central star.

The $H\beta$ flux can be described by

$$\begin{aligned} F_{H\beta} &= \frac{h\nu_{H\beta}\left(\int n_e n_p \alpha^{\text{eff}}_{H\beta} dV\right)}{4\pi D^2} && (2.5) \\ &= \frac{h\nu_{H\beta} n_e n_p \alpha^{\text{eff}}_{H\beta} R^3 \epsilon}{3D^2} && (2.6) \\ &= 4.12 \times 10^{-25}\ T_e^{-0.88} n_e n_p \frac{R^3 \epsilon}{3D^2}\ \text{W m}^{-2} && (2.7) \end{aligned}$$

where the numerator of Equation 2.5 is the number of $H\beta$ recombinations times the energy ($h\nu$) of each photon. $\alpha^{\rm eff}_{H\beta}$ is the effective recombination coefficient which describes the probability of recombination line emission (see Equation 2.42) and the volume integral is often assumed to be over a spherical nebular volume (as in Equations 2.6 and 2.7). In Equation 2.7, ϵ is the filling factor (see below), R is the radius of the nebula and D is the distance to the object.

The filling factor accounts for non-uniformity density of material within the region and appears in the volume integral. $\epsilon = 1$ describes a completely uniform medium which is often assumed for less complicated calculations or environments. $\epsilon < 1$ describes some degree of clumpiness in the medium.

The outer radius of the model ionized region is fit to observations by first assuming a uniform distribution of material ($\epsilon = 1$, which is the program default) and fitting the $H\beta$ flux. The filling factor is then lowered allowing the outer radius to increase out to fit observations. If $F_{H\beta}$ is held constant, Equation 2.6 varies as R^3 and ϵ. By decreasing the filling factor, the radius of the nebula will increase to compensate.

2.2.2 5 GHz Flux

While $H\beta$ flux emission suffers from extinction (see Section 2.4), radio emission at 5 GHz (6 cm) does not. The theoretical ratio between $F_{H\beta}$ and F_{5GHz} turns out to be independent of n_e and only weakly dependent on T_e. As a result, by observing emissions at 5 GHz, the true or expected $H\beta$ flux can be derived.

From Equations 3.24 and 2.7, we find

$$\frac{F_{5GHz}(Janksy)}{F_{H\beta}(Wm^{-2})} = 2.82 \times 10^6 t^{0.53} Y \tag{2.8}$$

where $t = T_e \times 10^{-4}$K and Y is a correction for the helium content which is defined in Equation 3.26.

Flux density at 5 GHz serves two purposes in modeling. It can be used to correct the $H\beta$ flux in sources that suffer from extinction. (Note that the value of extinction can also be derived from observations for both fluxes. See Section 2.4.) With no extinction to F_{5GHz}, the model predicted F_{5GHz} values can be compared directly to the observed values as a model constraint.

2.3 Magnitudes

The magnitude scale is a scale of brightness defined by

$$m_\nu - m_0 = -2.5 \times \log\left(\frac{F_0}{F_\nu}\right) \tag{2.9}$$

where m_0 and F_0 are the reference values for this system which are ideally calibrated such that an average A0 star has the same magnitude in all systems.

The magnitude being observed is m_ν at flux density F_ν. In practice, observations are made with a filter of some wavelength range centered on ν (See Section A.1.4). The observed flux density is found by taking the total flux over the whole filter and dividing by the filter width. Ideally, a narrow-band filter is used to maximize the accuracy of the value but a weighted averaging technique can be applied to broad-band filters to approximate the flux density.

Luminosity describes the total energy emitted by an object per unit time, or the power emitted. From Section 2.4, we know that flux is the energy per unit area per unit time. Luminosity, then, is the flux times the total area. For a spherical source of stellar radius R, the luminosity is given by

$$L = 4\pi R^2 F \tag{2.10}$$

where total stellar flux F is often approximated with a blackbody (Equation 3.20).

As with magnitude values, luminosity estimates must take into account the limitations of observing filters. The radius of the central star is also something that cannot readily be observed. The total stellar luminosity can be estimated by summing over observed flux density values across several filters:

$$L = 4\pi D^2 \sum_i f_\nu^i \omega_i \tag{2.11}$$

where D is the distance to the object from the observer. The total flux is estimated with the summation of the flux density for each filter (f_ν^i) times some weighting factor (ω_i) to allow for different filter widths.

From Equation 2.11, we can see that for a given distance to a PN and an assumed spectral shape, the flux density will be proportional only to the stellar luminosity. Then, in Equation 2.9, the flux density will be directly related to the magnitude. The models, therefore, are fit to the stellar V magnitude observations by adjusting the input stellar luminosity.

Note that these observed flux density values will need to be corrected for any extinction effects as we have discussed with $F_{H\beta}$ and F_{5GHz}.

2.4 Extinction

Extinction is a measure of how much flux density is lost through scattering or absorption while the radiation is traveling through space.

$$I_\lambda = I_{0_\lambda} e^{-\tau_\lambda} \tag{2.12}$$

where I_λ is the observed intensity, I_{0_λ} is the intensity if no extinction occurs and τ_λ is the optical depth at λ.

Optical depth at wavelength λ, τ_λ, is a measure of whether or not a photon (at wavelength λ) will be absorbed or scattered by the medium through which it travels. This will depend on how many particles are in the way (column density), how large each particle is (grain radius) and how likely the material is to absorb or scatter at that wavelength (Q_λ). A photon is more likely to hit something if it is either large or if there are many of them. A large optical depth ($\tau_\lambda > 1$) implies the photons are being largely absorbed or scattered by the medium. Such a medium is described as optically-thick. A small optical depth implies that there is little absorption or scattering of incoming photons and is referred to as optically-thin.

The increment of optical depth along the line of site is defined by

$$d\tau_\nu \equiv -\kappa_\nu(l)dl \tag{2.13}$$

where absorption coefficient κ_ν describes the energy absorbed or scattered by the medium and l is the path length.

In practice, τ_λ can be expressed as:

$$\tau_\lambda = cf(\lambda) \tag{2.14}$$

where $f(\lambda)$ is the standard extinction curve, a wavelength dependent function that observations have shown is essentially the same for all stars. Only the total amount of interstellar extinction depends on the star and is determined by the constant c. The data from Rieke & Lebofsky (1985) are adopted for the standard extinction curve (SEC) for our models. Studies have shown that the largest deviation in the f_λ wavelength function occurs at short (UV) wavelengths. As a result, the extinction applied in the models may not adequately fit with observations at these wavelengths.

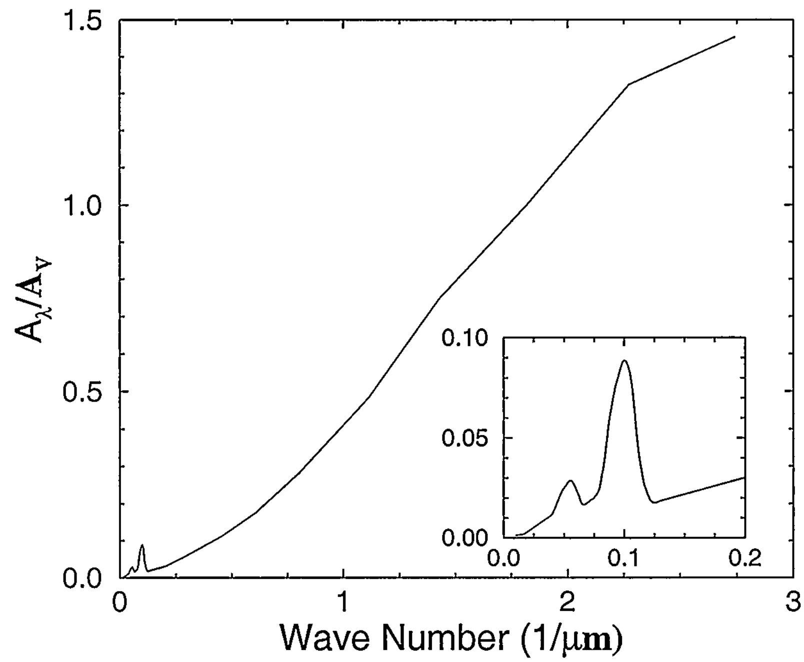

Figure 2.1: The standard extinction curve from Rieke and Lebofsky (1985).

The increase in apparent magnitude of an object, which results from extinction is called the *total extinction.*

$$A_\lambda = m_\lambda - M_\lambda + 5 - 5\log D. \tag{2.15}$$

Substituting πF_λ for I_λ in Equation 2.12, the value of c for a given nebula can be derived by comparing the expected flux and an observed value by the equation,

$$cf(\lambda) = log\left(\frac{F(\lambda)_{exp}}{F(\lambda)_{obs}}\right). \tag{2.16}$$

This method assumes a standard extinction curve and that the source of extinction is outside the nebula.

For an optically-thin radio continuum and with no extinction for the $H\beta$ flux, there is only a small temperature dependence with no density dependence in the $H\beta$-5GHz flux ratio (see Equation 2.8). Thus, the expected $H\beta$ flux can be calculated through observations of the radio continuum. A common method to calculate the extinction of a given PN is to use Equation 2.16 for $H\beta$. Comparing the derived $c(H\beta)$ to the standard extinction curve gives a value for the total extinction for the PN.

$$\begin{aligned} c(H\beta) &= 0.4A_{H\beta} && (2.17)\\ &= 0.4\left(\frac{A_{H\beta}}{A_V}\right)_{SEC} A_V && (2.18)\\ &= 0.4(1.17)A_V && (2.19)\\ &= 0.47A_V && (2.20) \end{aligned}$$

where $\left(\frac{A_{H\beta}}{A_V}\right)_{SEC}$ is the value from the standard extinction curve at $H\beta$.

The colour excess is another measure of extinction in the direction of an object.

$$E_{B-V} = (B-V) - (B-V)_0. \tag{2.21}$$

Here, $(B-V)$ is the difference between the magnitude in blue (B) and visual (V) for a single source. The colour excess measures the difference between (B−V) for the object and for a similar unobscured object. This method requires direct observational data of the magnitudes, which are often measured for stellar sources. This method is most often used for stars.

Another method of determining extinction is by taking ratios of line intensities at different wavelengths having little or no temperature or density dependencies. In general, this is the case for any set of lines that originate from the same upper level, but most often the Balmer lines are used since they are the most frequently observed.

From Equation 2.16 and again using a standard extinction curve, we can derive the total extinction by observing $H\alpha$ and $H\beta$.

$$\left(\frac{H\alpha}{H\beta}\right)_{obs} = 10^{c(H\beta)-c(H\alpha)} \left(\frac{H\alpha}{H\beta}\right)_{exp} \tag{2.22}$$

For the interstellar medium, the value for $H\beta/\ H\alpha = 2.85$ is standard for Case B at 10,000K and $n_e = 10^4$ cm^{-3}. By observing a value for the ratio, the value of A_V can be determined.

$$\begin{aligned}
c(H\beta) - c(H\alpha) &= 0.4(A_{H\beta} - A_{H\alpha}) && (2.23)\\
&= 0.4\left(\frac{A_{\lambda=H\beta}}{A_V}\right)_{SEC} A_V - \left(\frac{A_{\lambda=H\alpha}}{A_V}\right)_{SEC} A_V && (2.24)\\
&= 0.4\left[\left(\frac{A_{\lambda=H\beta}}{A_V}\right)_{SEC} - \left(\frac{A_{\lambda=H\alpha}}{A_V}\right)_{SEC}\right] A_V && (2.25)\\
&= 0.4(1.17 - 0.80)A_V && (2.26)\\
&= 0.148A_V && (2.27)
\end{aligned}$$

where the two terms in square brackets in Equation 2.25 are the values from the standard extinction curve at the appropriate wavelengths.

By assuming that extinction goes to zero at infinite wavelength, we find the average interstellar extinction has

$$R = \frac{A_V}{E(B-V)} = 3.1. \tag{2.28}$$

Interstellar extinction is calculated in a separate program written by K. Volk which applies the standard extinction curve to the output spectrum for the observed $E(B-V)$ value for the PN.

2.5 Zanstra Temperatures

The temperature of the central star in planetary nebulae (CSPN) is important in defining the photoionization energy as is the stellar atmosphere model which will be discussed in Section 3.2.2. While there is no means to directly observe the stellar temperature, the Zanstra method has proven very reliable in determining a value from observations.

The derivation for the Zanstra method of finding stellar temperatures relies on a balance of the number of photons emitted by the star capable of ionizing the nebula and the number of recombinations that result. This discussion of a simple balance photoionization-recombination scenario and the derived Zanstra temperatures follows from Kwok (2000) and Pottasch (1984).

Total recombinations are assumed to be balanced with the total number of ionizing (UV) photons emitted by the central star for an ionization bounded system. The *number of ionizing photons* is

$$Q_{photon} = \int_{\nu_1}^{\infty} \frac{4\pi R_*^2 \pi B_\nu(T_*)}{h\nu} d\nu. \tag{2.29}$$

This is derived from the total energy at frequency ν from the star assuming a blackbody spectrum (the area at radius R_* times the flux of a blackbody at T_*) divided by the energy of a single photon at that wavelength. ν_1 is the frequency of the Lyman limit which is the minimum energy required to ionize the hydrogen atom from the ground state. By substituting the equation for a blackbody (Equation 3.20) and letting

$$x(\nu) = \frac{h\nu}{kT_*} \tag{2.30}$$

Q_{photon} becomes

$$Q_{photon} = 8\left(\frac{\pi R}{c}\right)^2 \left(\frac{kT_*}{h}\right)^3 \int_{\frac{h\nu_1}{kT_*}}^{\infty} \frac{x^2}{e^x - 1} dx. \tag{2.31}$$

We define

$$G(T_*) = \int_{\frac{h\nu_1}{kT_*}}^{\infty} \frac{x^2}{e^x - 1} dx. \tag{2.32}$$

where $G(T_*)$ effectively governs the total number of photons.

For a stellar atmosphere that radiates as a blackbody at temperature T_*, the stellar luminosity can be expressed as

$$L_* = 4\pi R_*^2 \sigma T_*^4 \tag{2.33}$$

with

$$\sigma = \frac{2\pi^5 k^4}{15h^3c^2} \tag{2.34}$$

defining the Stefan-Boltzmann constant. By substituting Equations 2.33 and 2.34 into Q_{photon} (Equation 2.31), the final form of the ionizing photon count is

$$Q_{photon} = \frac{15G(T_*)L_*}{\pi^4 kT_*}. \tag{2.35}$$

The *total number of recombinations* to levels above the ground state is given by

$$Q_{recomb} = \int n_p n_e \alpha_B dV \tag{2.36}$$

where α_B is the recombination coefficient for Case B, which is described in the next section (Eqn. 2.39) and is a particle-velocity-dependent function. Assuming a spherical geometry, a uniform density distribution and that a completely ionized region composed of hydrogen will satisfy $n_e = n_p = n_H$,

$$Q_{recomb} = n_H^2 \alpha_B \left(\frac{4}{3}\pi r_s^3\right) \tag{2.37}$$

where r_s is the Strömgren radius that describes the volume containing all the ionized material. Beyond this radius, the nebula quickly becomes neutral. We equate Equations 2.37 and 2.35 to find the energy balance for such an ionization bounded region.

The most commonly used equation to calculate the Zanstra temperature is a ratio of the $H\beta$ flux and the stellar V magnitude. For a blackbody, the stellar flux density at V is $F_\nu = \pi B_\nu(T_*)$. From $H\beta$ flux Equation 2.5, recognize that $Q_{recomb}\alpha_{H\beta}^{eff}/\alpha_B$ is the term in parentheses. Then, with Equations 2.5, 3.24, 2.37 and 2.35, the ratio becomes

$$\frac{F(H\beta)}{F_\nu} = \frac{15h\nu_{H\beta}}{\pi^5 k B_\nu(T_*)}\sigma\frac{\alpha_{H\beta}^{\rm eff}}{\alpha_B}T_*^3 G(T_*). \tag{2.38}$$

The *recombination coefficient* defines the probability of an electron recombining with a proton or ion.

$$\alpha_{nl}(T_e) = \int_0^\infty \sigma_{nl} v f(v) dv \tag{2.39}$$

where n is the quantum number, l the angular momentum quantum number and v is the electron velocity. The velocity distribution, $f(v)$, is the Maxwellian velocity function which is assumed for LTE systems such as the plasma in PNe and is dependent on the kinetic temperature (the electron temperature, in this case) and is defined by:

$$f(v) = \frac{4}{\sqrt{\pi}}\left(\frac{m_e}{2kT_e}\right)^{\frac{3}{2}} v^2 e^{-m_e v^2/2kT_e}. \tag{2.40}$$

The *recombination cross-section* is

$$\sigma_{nl}(v) = \left(\frac{16e^2h}{3\sqrt{3}m_ec^3}\right)\left(\frac{\nu_1}{\nu}\right)\left(\frac{h\nu_1}{\frac{1}{2}m_ev^2}\right)\left(\frac{g_{bf}}{n^3}\right) \tag{2.41}$$

where g_{bf} is the bound-free Gaunt factor which corrects for a classical treatment of quantum mechanical effects. g_{bf} has a small temperature dependence but at short wavelengths, $g_{bf} \approx 1$ and so σ_{nl} has essentially no T_e dependence.

The total recombination coefficient is a sum over all energy levels (n and l) of Equation 2.39. For Case A systems (where the nebula is optically thin to the Lyman continuum), the sum includes the ground state ($n = 1$). For the ionization bounded Case B where the nebula is optically thick to the Lyman continuum, the ground state is not included and the sum begins at $n = 2$. All photons decaying to the $n = 1$ (Lyman) energy level will be quickly reabsorbed by the nebula and outside the ionized region no Lyman series photons except Lyman α will be observed.

The *effective recombination coefficient* is somewhat of a misnomer in that it describes the probability of emitting a recombination line, or the probability of cascading as a result of a spontaneous decay following a successful recombination.

$$\alpha^{eff}_{nl,n'l'} = \frac{n_{nl}A_{nl,n'l'}}{n_pn_e} \tag{2.42}$$

where $A_{nl,n'l'}$ is the Einstein A value or the probability of spontaneous decay from upper level nl to level $n'l'$. n_{nl} is the population density of the upper level which is determined by the Saha and Boltzmann equations. The Saha equation describes the probability of being ionized to some degree and Boltzmann describes the probability of being in an excited state within a given state of ionization. The level population density also has an n_pn_e dependence, which effectively removes the dependence from α^{eff}.

The population density equation is

$$n_{nl} = b_{nl} n_p n_e (2l+1) \left(\frac{h^2}{2\pi m_e k T_e} \right)^{\frac{3}{2}} e^{-h\nu_n / kT_e} \tag{2.43}$$

where the factor of $(2l+1)$ is the statistical weight and b_{nl} is the "degree of departure from the thermodynamical equilibrium distribution" (Kwok 2000). $b_{nl} = 1$ for thermodynamical equilibrium.

Note that Equations 2.40 and 2.43 have similar temperature dependencies. Looking back at the Zanstra temperature equation (2.38), we see that the ratio of recombination and effective recombination coefficients will have no T_e dependence, leaving the T_e^3 term as the only undetermined quantity on the RHS.

The LHS of Equation 2.38 is in practice a ratio of observed fluxes. F_ν is derived from the stellar magnitude (Equation 2.9) observations while $F_{H\beta}$ can be observed directly or found through radio observations at 5 GHz if significant extinction occurs at $H\beta$.

The above derivation is for hydrogen Zanstra temperatures which assumes complete absorption of photons shortward of 912 Å (ionization bounded case B) and emission of $H\beta$ photons. Zanstra temperatures can in fact be derived given any stellar magnitude observation and an appropriate line flux for any given element following the same principles. For instance, helium Zanstra temperatures assume complete absorption of photons shortward of 228 Å and the emission of HeII (4684 Å) photons. The presence of helium can complicate calculations by absorbing and emitting photons which would ionize nebular H. The effects of H-He coupling are in general assumed to be negligible. However, note that the coupling effects are more significant for HeI and the Zanstra temperature derived from HeI is typically less reliable as a result. If the H and the He Zanstra temperatures are the same, it implies that the nebula is optically thick and the central star is radiating as a blackbody.

Derived Zanstra temperatures reflect errors based on the assumption of a blackbody spectrum for the source and by neglecting any effects of dust within the Strömgren radius. Further, the method assumes accurate stellar magnitude and $H\beta$ or 5 GHz emission observations and is only as reliable as those observations.

Zanstra temperatures derived from observed values are used as a model input parameter, then the input stellar luminosity is adjusted to fit the observed stellar V magnitude. From the output, the model Zanstra temperatures (H and He) are calculated. The observed and model values are compared to assess the success of the model.

2.6 Distance Estimates to PN

Another important measurement to characterize PNe is the distance to the nebula. There are many methods to calculate the distance and the most useful methods are presented here.

Masson (1986, 1989) derived the distance to NGC 7027 by measuring the angular expansion rate of the nebula and comparing the results to the velocity maps for the nebula. Angular and linear values are related to the distance by the equation:

$$R = \frac{D\theta}{206,265} \tag{2.44}$$

where R is the radius of the nebula (in pc), θ is its angular radius (in arcseconds), and D is the distance to the nebula (in pc). Therefore, high quality nebular maps at different times should reveal good distance values.

Distance can also be derived from the interstellar extinction but the method relies on the nebula being close to the galactic plane and that there are enough stellar objects with known distances nearby to be able to determine the extinction versus distance relationship. Since extinction is a function of the total optical depth (Equation 3.3) which is in turn a function of distance, the distance to the nebula can be derived from the extinction. The extinction relationship is determined by taking measurements of several objects in the same region of the sky and assuming a uniform density of material out to the source.

Another method involves the $H\beta$ flux and forbidden line ratios (Pottasch 1984). By looking at the $H\beta$ flux equation (Eqn 2.7), an equation can be derived for electron density, n_e, which depends on $H\beta$ flux, angular radius, electron temperature, filling factor and distance. The first two variables can be measured. n_e and T_e can be derived from forbidden line ratios (Section 3.2.3). The filling factor is an unknown quantity but is assumed to be unity for a nebula with a uniform appearance and 0.5 for a nebula which appears "half full". The distance can then be calculated.

The 21 cm hydrogen line is a weak hydrogen line emitted in the radio wavelength range where the extinction is very small. The absorption strength depends on hydrogen density (n_H), the temperature of the ISM (T_{ISM}) and the distance to the nebula. n_H and T_{ISM} are both approximately known which leaves the derivation of the distance.

The Shlovsky distance uses a statistical method for determining the distance which assumes an ionization bounded nebula and that the mass of the ionized region is the roughly the same for all PNe. The method requires measured values of the angular radius of the nebula and the any λ-dependent emissivity relation involving

n_e and n_p (where we assume $n_e = n_p$), such as flux density (e.g. 5 GHz) or line flux (eg. $H\beta$), which also does not suffer from or can be corrected for extinction. It is then assumed that the mass of the ionized region can be described by:

$$M = \left(\frac{4}{3}\pi R^3 \epsilon\right) \; n_e \mu_e m_H \tag{2.45}$$

where μ_e is the mean mass per particle, ϵ is the filling factor and m_H is the mass of a hydrogen atom.

Combining Equation 2.45 and Equation 2.3 for flux density and also recalling that the nebular radius and distance are related by $R = \theta D$, the distance can be calculated with the following equation:

$$D = \left(3\alpha_\nu^{eff} h\nu\right)^{1/5} \theta^{-3/5} \epsilon^{-1/5} F_\nu^{-1/5} \left(\frac{M}{4\pi \mu_e m_H}\right)^{2/5} . \tag{2.46}$$

This method is surprisingly useful considering the mass of the ionized region varies greatly in PNe.

Distance measurement methods rely heavily on approximations of quantities or high-quality measurements of various nebular parameters. This leads to a large range of estimated distances for nebulae. The distance to NGC 7027 has estimates from 178 pc to 1.8 kpc. IC 418 has distance estimates ranging from 0.42 kpc to 1.8 kpc. Careful studies have been able to place more accurate upper and lower limits to these estimates, but distance remains one of the more difficult PN quantities to measure.

2.7 Line Diagnostics

Since PN environments are of a density high enough for collisional excitation of electrons among the heavier atoms but sufficiently low to allow the spontaneous emission probability to be larger than the collisional counterpart, spontaneous decays are favoured. Forbidden line emissions which are of interest in PN all share two basic electron configurations, np^3 (such as for [OII]) and np^2 (such as for [OIII]).

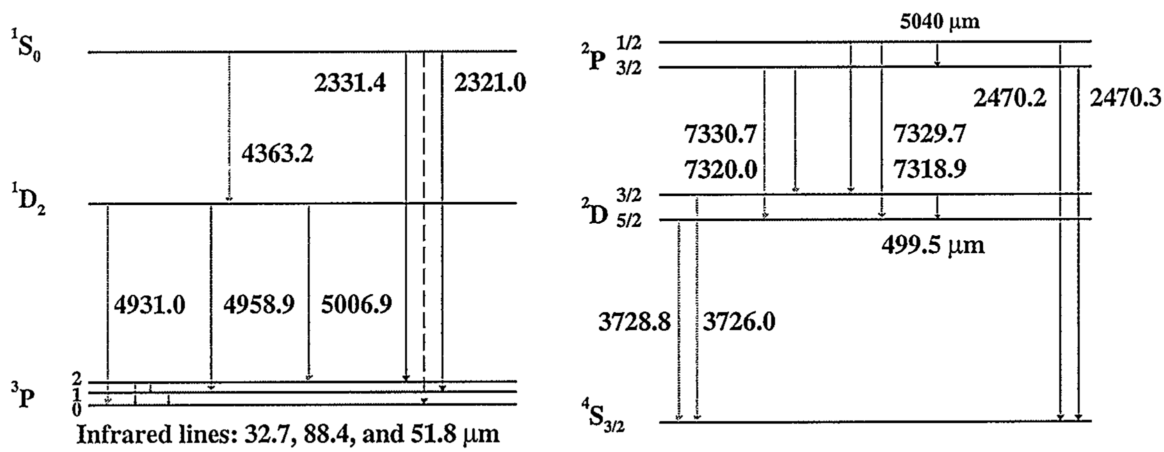

Figure 2.2: [OIII] (on the left) has an np^2 configuration with three multiplets in the ground state and none in the upper two levels. [OII] (on the right) is the np^3 with a single-level ground state but with the next two levels each split into two multiplets.

Fine structure lines are a result of transitions within the same multiplet which is the degeneracy of an energy level due to spin-orbit interactions. In the np^2 configuration, the lower three levels are a multiplet and the upper levels in np^3 have a pair of multiplets.

Populations of different energy levels (S, P or D in Fig. 2.2) are sensitive to temperature since the energy gaps are relatively large compared to the gaps between multiplets. As a result, ratios of transition strengths that originate from different energy levels will indicate the temperature of the electrons. On the other hand, the energy required to excite electrons into any level within a multiplet is similar. It is the electron density that determines the strength of the fine structure lines radiating from the multiplet. The difference in transition strengths of the forbidden lines can be used as electron density (Section 2.7.3) or electron temperature probes (Section 2.7.2).

2.7.1 Collision Coefficient

The fundamental equation for the collision coefficient takes the same form as the recombination coefficient in Equation 2.39 with the collision cross section σ_{nl} instead of the recombination counterpart. The cross-section is again a quantum quantity with a Maxwellian energy distribution.

$$\sigma_{nl}(v) = \left(\frac{\pi h^2}{4\pi^2 m_e^2 v^2}\right)\frac{\Omega_{ji}}{g_j}$$

where the collision strength is

$$\Omega_{ji}(J) = \frac{(2J+1)}{(2L+1)(2S+1)}\Omega_{ji}$$

The collision coefficient has the form

$$C_{ji} = \frac{8.629 \times 10^{-6}\Omega_{ji}}{\sqrt{T_e} g_j} e^{-E_{ij}/kT_e} \mathrm{cm}^3\mathrm{s}^{-1}. \tag{2.47}$$

The collision rate is the probability of a collision (the collision coefficient) times the electron density.

2.7.2 Temperature Diagnostics

Since the upper levels (P and D in the np^3 configuration and S and D for np^2 in Figure 2.2) have larger energy separations, a higher kinetic temperature is required to populate the levels. The T_e diagnostic involves a ratio of populations for the line emissions originating from each of these upper levels.

By considering the detailed balance for each level and the statistical equilibrium equations for transitions into and out of each level, the line ratio can be described by the collisional (C_{ji}) and spontaneous (A_{ji}) transition coefficients and the line frequencies. The resultant ratio will retain the temperature dependence from the exponential term of the collision coefficient (Equation 2.47), but lose any density dependent terms.

For example, from the [OIII] ion,

$$\frac{I(4363\ \text{Å})}{I(5007\ \text{Å} + 4959\ \text{Å})} = 0.132 \times e^{-32990K/T_e}. \tag{2.48}$$

This equation is valid for the low density limit where every collisional excitation results in a spontaneous decay. The temperature dependence will still be the stronger effect for these line ratios in PN.

2.7.3 Density Diagnostics

Unlike the temperature probe, the density diagnostics rely on the fine structure line emissions from any of the multiplets found in the five-level atom. These multiplets have small energy separations in comparison and have a negligible temperature dependence in the system. The population variations of each level within a multiplet are a result of the electron density of the nebula.

The lower level of the np^2 configuration is split into three separate levels which have small energy differences very close to the ground state. They are dominated by collisional excitation since they are very close to the ground state which makes them ideal for this discussion. In the np^3 configuration, either of the upper levels (D or P) can be considered a two-level atom with the ground state at any given temperature since the energy separation is small. Ratios of lines originating from each level of the same multiplet can be used for density diagnostics. In either case, the populations in each of the multiplet levels will be dependent on the electron density. The ratio of the respective line strengths will be indicative of the level population which in turn will reveal the electron density.

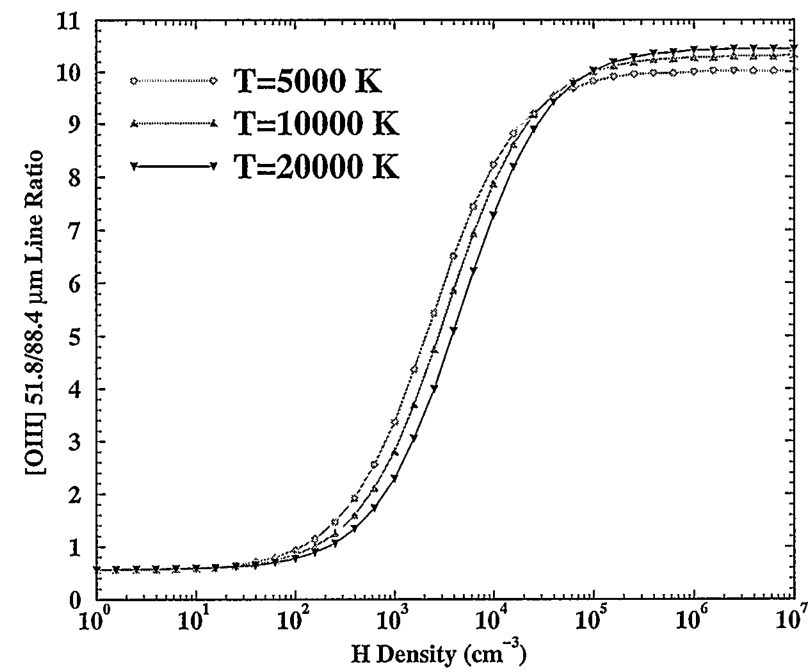

Figure 2.3: The density diagnostic curve for the 51.8/88.4 line ratio in [OIII] for three different electron temperature models (produced by Cloudy). The electron temperature demonstrates little effect on the diagnostic ability of the relationship.

Figure 2.3 shows the temperature dependence for the [OIII] transitions which is negligible. A definite density dependence, however, can be seen between 100 cm^{-3} and 10^5 cm^{-3}. Observed 51.8/88.4 μm line ratios falling in the appropriate range can be used as a fairly accurate electron density probe.

The density limits are established by recognizing that in a high density regime, the collisional effects will greatly outweigh the spontaneous decays and the level populations become independent of n_e. In the low density limit, every collisional excitation will be followed by a spontaneous decay before another collision occurs so the line ratio only depends on the Einstein coefficients. In the intermediate region, the ratio depends on the population density of each upper level and the respective Einstein coefficients.

A set of detailed balance and statistical equilibrium equations similar to the temperature diagnostics are used to derive the equation for the line ratios. The exponential temperature dependence in Equation 2.47 will vanish for the small energy separation term compared to typical nebular plasma temperatures.

Line diagnostics are used both in establishing input parameters for our models as well as in comparing our results to observations. Observational values for electron temperature and density are generally derived with ratios of observed line fluxes. We also use the model flux densities to find T_e and n_e for the final model to measure the success of as well as to identify weaknesses in the computer models presented in this work.

Chapter 3

Computer Modeling

This chapter outlines the methods used to create the computer models of PNe spectrum. The creation of the dust opacity files which define the interactions between the grains and the surrounding radiation field is discussed in Section 3.1. The physics and input parameters of Cloudy which models the ionized region of the PNe and DUSTCD which models the neutral dust shell are discussed in Sections 3.2 and 3.3 respectively.

3.1 Dust Grain Opacity

In order to create the dust opacity files, a series of smaller service computer programs written by K. Volk were used. The first one uses Mie Theory to calculate the extinction coefficients Q_ν (Section 3.1.1) and $\pi a^2 Q_\nu$ values for dust grains with a given index of refraction and size for a given wavelength range of interest. Index of refraction values for AMC by Rouleau and Martin (1991) were used. While the Mie Theory is used to calculate the opacity function of a given dust grain, it should be noted that grains are not expected to be spherical given the harsh environments in which they exist in PNe, but rather the amorphous nature of the grains would suggest random shapes and sizes. A solution using ellipsoidal grains would not likely be more representative of such a lumpy grain. In general, grains are modeled with a spherical symmetry since there is no exact solution to the Mie Theory applied to non-spherical grains.

If dust features are to be included, they will be added to the rebinned set of $\pi a^2 Q_\nu$ values. The features are defined as "strengths" relative to the continuum:

$$Q_\nu(feature) = Q_\nu(continuum) * (1 + f_\nu) \tag{3.1}$$

where f_ν is the input feature strength at ν. The normalized feature profiles are shown in Figure 1.6.

The output data file is formatted to be the input file for DUSTCD (Section 3.3.4) which has a different wavelength grid than required by Cloudy. The final step is to take the extinction efficiency values and calculate the absorption and scattering cross-sections for input to Cloudy.

3.1.1 Mie Theory

Interactions between the PN radiation field and dust grains is characterized by the optical depth at frequency ν (τ_ν) of the grains (see Section 2.4). For dust, the absorption coefficient is

$$\kappa_\nu = \pi a^2 Q_{ext}(\nu) N(a). \tag{3.2}$$

The optical depth defined by Equation 2.13 can then be expressed as:

$$\tau_\nu = \int_0^L N(a) \pi a^2 Q_{ext}(\nu) dl \tag{3.3}$$

where L is the thickness of the medium, l the path length, $N(a)$ is the density of particles and the extinction efficiency (Q_{ext}) describes the degree to which the absorption or scattering takes place within the medium at a given frequency ν. Q_{ext} is a dimensionless number which is the sum of the absorption and scattering components, $Q_{ext}(\nu) = Q_{abs}(\nu) + Q_{scat}(\nu)$. Q_{abs} approximates 1 (and $Q_{ext} \sim 2$) when the radius a is much larger than the wavelength of the interacting photons. If the wavelength-radius condition does not hold, then the extinction efficiency is found with the Mie Theory.

Mie Theory is a spherically symmetric solution to Maxwell's equations. The following discussion is based on unpublished ISM notes of Volk (2000). The extinction efficiency coefficients are calculated starting from the index of refraction, m, for the different types of dust with radius a:

$$\begin{aligned} m &= n - \imath k && (3.4) \\ &= \sqrt{\left(\frac{\epsilon(\omega)}{\epsilon_0} - \imath\frac{\sigma(\omega)}{\omega\epsilon_0}\right)} && (3.5) \end{aligned}$$

where ϵ is the dielectric constant and σ is the conductivity at frequency $\omega = 2\pi\nu$. n and k are the real and complex coefficients of the index of refraction defined by σ and ω in Equation 3.5. The resultant scattering wave is a product of spherical harmonics in angle and a spherical Bessel function in radius with electromagnetic boundary conditions. The solution is expressed in terms of $x = 2\pi a/\lambda$ and $y = mx$ (values for x are listed in the dust opacity files produced by the code).

$$Q_{ext} = \frac{2}{x^2}\sum_{\jmath=1}^{\infty}(2\jmath+1)\left(|a_\jmath|^2 + |b_\jmath|^2\right) \tag{3.6}$$

$$Q_{scat} = \frac{2}{x^2}\sum_{\jmath=1}^{\infty}(2\jmath+1)\left(\Re\left(a_\jmath + b_\jmath\right)\right) \tag{3.7}$$

where $a_\jmath$ and $b_\jmath$ are the complex coefficients of the spherical harmonics. $a_\jmath$ and $b_\jmath$ are determined by a pair of recurrence relations ($\alpha_\jmath(x)$ and $A_\jmath(y)$, below) which are functions of x and y.

$$\alpha_j(x) = \frac{2j-1}{x}\,\alpha_{j-1}(x) - \alpha_{j-2}(x) \tag{3.8}$$

$$A_j(y) = -\frac{j}{y} + \frac{1}{j/y - A_{j-1}(y)} \tag{3.9}$$

such that

$$a_j = \frac{[A_j(y)/m + j/x]\, \Re\{\alpha_j(x)\} - \Re\{\alpha_{j-1}(x)\}}{[A_j(y)/m + j/x]\, \alpha_j(x) - \alpha_{j-1}(x)} \tag{3.10}$$

$$b_j = \frac{[mA_j(y) + j/x]\, \Re\{\alpha_j(x)\} - \Re\{\alpha_{j-1}(x)\}}{[mA_j(y) + j/x]\, \alpha_j(x) - \alpha_{j-1}(x)} \tag{3.11}$$

In the small size limit (when a is small compared to λ), the Q results become

$$Q_{ext} = -\Im\left(4xM + \frac{4}{15}M^2\frac{m^4 + 27m^2 + 38}{2m^2 + 3}\right) + x^4\Re\left(\frac{8}{3}M^2\right) \tag{3.12}$$

$$Q_{scat} = x^4\frac{8}{3}|M|^2 \tag{3.13}$$

where $M = (m^2 - 1)/(m^2 + 2)$.

For the $a >> \lambda$,

$$Q_{ext} = 2 \tag{3.14}$$

$$Q_{scat} = 1 + \omega \tag{3.15}$$

$$Q_{abs} = 1 - \omega \tag{3.16}$$

and ω is the albedo of the grain. *Albedo* is the ratio of radiation scattered by the grain to the radiation incident on the grain. Scattering of all the incident radiation is described by an albedo of 1. Grain albedo of 0 describes the total absorption of all incident radiation.

3.2 Modeling the Ionized Region

The software program Cloudy by G. Ferland is used to model the ionized region of the nebula. The model nebula is divided into layers with the emerging radiation field of one layer becoming the incident radiation field for the next layer. The central star provides the incident field for the first layer. The final layer provides either the output spectrum or the incident radiation field for the neutral dust shell, if present.

Cloudy assumes an electron temperature, T_e, then uses ionization balance to find the electron density, n_e. Detailed energy balance with n_e is used to calculate T_e for the ionized region. This new electron temperature is used to recalculate n_e. The processes is repeated until the values are consistent.

3.2.1 Ionization Balance Equation

Balancing photoionization and recombination effects provides one part of the physics necessary for finding the electron density n_e in the ionized region. The balance is taken for each atom in each ionization state.

$$N_1(X^i) \int_{\nu_i}^{\infty} \frac{4\pi J_\nu}{h\nu}\, a_1(\nu, X^i) = \sum_{j+1}^{\infty} N_j(X^{i+1}) n_e \alpha_j(T_e, X^i) \tag{3.17}$$

where X is some atom and i is its ionization state. N_j is the number density of the atom in the j^{th} excited state with $j = 1$ describing the ground state. a_1 is the cross section for photoionizing the atom X from the ground state. α_j is the recombination coefficient (Equation 2.39) which describes the probability of a recombination between the atom and an electron with velocity v.

Total number density $n_e(X)$ contributed from each atom X is given by

$$n_e(X) = \sum_{i=1}^{p_X} n_i N(X_i) \tag{3.18}$$

where n_i is the number of electrons from each atom in the i^{th} ionization state for the atom, $N(X_i)$ is the number density of the atom in the i^{th} state and p_X is the number of ionization states for each atom. The total number density of element X is calculated from:

$$N(X) = \sum_{i=1}^{px} N(X_i) \tag{3.19}$$

where $N(X_i)$ is the number density of the atom X in ionization state i.

3.2.2 Energy Balance in Thermal Equilibrium

For energy balance, we want to balance all the heating processes with all the cooling processes in the system. The following sections discuss the main processes included in the energy balance equations and is based on discussions in Kwok (2000) and Pottasch (1984). The various abundances derived through the ionization balance equations (as described in the previous section) are used here in search of the electron plasma temperature, T_e.

The method involves a strict detailed balance of processes and the calculations are based on the difference between heating and cooling for each pair of processes which is a numerically more stable algorithm.

Photoionization: stellar emission

Stellar radiation provides the dominant radiation source, mainly in the UV range. This and the diffuse field (see Section 1.1) are assumed to be the only sources for the ionization of the nebula.

The most common stellar atmosphere approximation is that of a blackbody. Planck's Distribution Law is an adequate approximation for photons in a high-density regime like those of stellar interiors. The central star of NGC 7027 has been modeled as a blackbody at 198,000 K.

$$B_\nu = \frac{2h\nu^3}{c^2}\frac{1}{e^{h\nu/kT_*} - 1} \tag{3.20}$$

where T_* is the temperature of the star.

For situations where the blackbody is an overly idealized model, more complex models need to be adopted. For IC 418, we adopted the Kurucz atmosphere models which are line-blanketed, LTE atmospheric models. Line-blanketing uses all the line information possible to create a more detailed stellar continuum. Figure 3.1 compares a Kurucz model atmosphere at 41,000K with the equivalent blackbody spectrum.

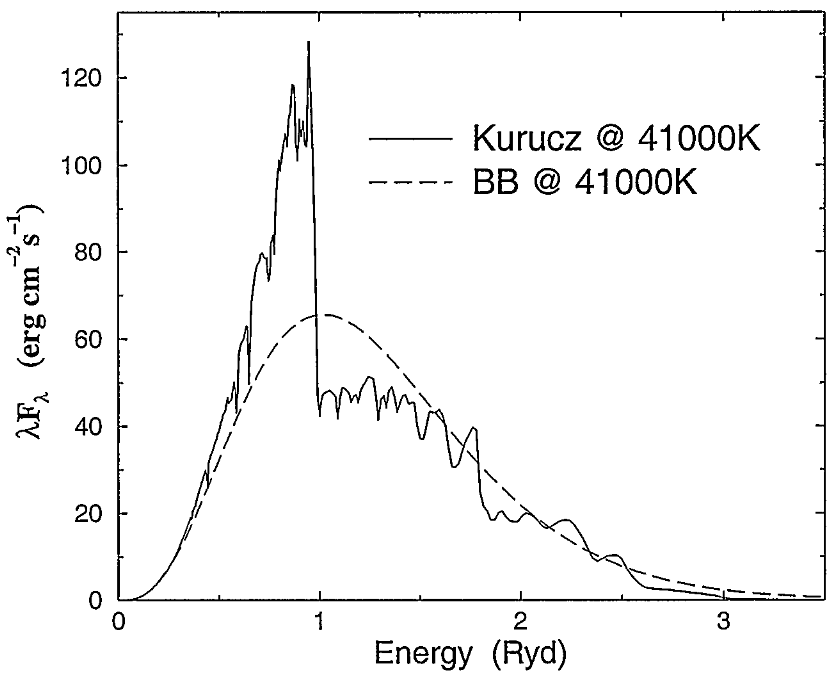

Figure 3.1: The Kurucz stellar atmosphere model at 41000K as produced by Cloudy. The equivalent blackbody spectrum is plotted for comparison. The rydberg (Ryd) is described in Appendix A.2.1.

The Kurucz model has much more energy at the longer wavelengths compared to the blackbody of the same temperature ($T_{bb} = T_k$). The blackbody at T_k tends to match the model along the higher energies (the right side of Fig. 3.1) but to greatly underestimating the peak and over-producing ionizing photons because it is above the model curve at E$\sim$1 Ryd.

These stellar models are especially important for lower temperature stars where the blackbody approximation becomes less appropriate. The blackbody peak and the Lyman jump are both at 1 Ryd which is where the output differences of the two models is the most significant. At higher temperatures, the blackbody peak shifts away from this jump and the effects are not as noticeable. As a result of the central star temperature of 41,000 K in IC 418, we used the Kurucz model (See Section 4.2.1).

Plane-parallel model atmospheres are defined by the effective temperature of the star and the surface gravity ($g_s = GM/R^2$, normally quoted in log format).

Recombination: bound-free radiation

Since there is a larger energy gap between the lower levels in H and He than in heavier elements, collisional excitation of H and He is less favourable in a PN environment. Instead, their emission contribution is produced through the recombination of a free electron with a proton or ion.

The capture of an electron with some speed v by a proton (or hydrogenic ion) to some level n is marked by the release of a photon with energy equal to

$$h\nu = \frac{1}{2}m_e v^2 + \frac{h\nu_1}{n^2}. \tag{3.21}$$

where ν_1 is the frequency of the Lyman limit (3.3×10^{15} Hz). The Lyman limit defines the minimum energy required for an electron in the ground state of a hydrogen atom to escape.

This process in nebular hydrogen and helium dominates in the optical range and the total emissivity is given by:

$$4\pi j_\nu(bf) = 2.16 \times 10^{-33} \frac{n_e n_p}{T_e^{\frac{3}{2}}} \sum_{n'}^{\infty} \frac{g_{bf}}{n^3} e^{h(\nu_n - \nu)/kT_e} \text{ W m}^{-3} \text{ Hz}^{-1} \tag{3.22}$$

where g_{bf} is the bound-free Gaunt Factor which corrects for the classical treatment of quantum mechanical effects.

Bremsstrahlung (free-free) Radiation

A free electron passing near an ion without recombining will be accelerated and radiate a photon. The resultant emission is dependent on the energy (speed) of the electron and its distance from the ion.

$$4\pi j_\nu(ff) = 6.84 \times 10^{-39} n_i n_e T_e^{-\frac{1}{2}} g_{ff}(\nu, T_e) e^{-h\nu/kT} Y \text{ W m}^{-3} \text{ Hz}^{-1} \tag{3.23}$$

$$= 10.3 \times 10^{-39} T_e^{-0.35} \nu^{-0.1} n_e n_i Y \text{ W m}^{-3} \text{ Hz}^{-1} \tag{3.24}$$

where n_i is the number density of the atom and the free-free Gaunt Factor, g_{ff}, is taken to be equal to 1 except in radio frequencies where it is defined by

$$g_{ff}(\nu, T_e) = \frac{\sqrt{3}}{\pi} \left[17.7 + \ln \left(\frac{(T_e)^{3/2}}{\nu \, Z} \right) \right], \tag{3.25}$$

where Z is the nuclear charge.

$$Y = 1 + \frac{n(He^+)}{n_p} + 3.7 \frac{n(He^{++})}{n_p} \tag{3.26}$$

is a correction for the presence of all forms of helium.

Free-free radiation is stronger than bound-free radiation in the infrared and dominates in the radio spectrum.

Two-Photon Radiation

Two-photon radiation results from electrons that are in the 2S level of a hydrogen atom. Transitions directly to the 1S ground state are forbidden since they violate the Laporte parity rule ($\Delta l = \pm 1$). They can be photoionized out, collisionally excited into the 2P state or some other state or can decay down to the 1S ground state via the release of two photons. In low density regimes, like PN, it is more favourable for a 2S electron to decay to a metastable state somewhere between the n=1 and n=2 levels (ν_1) and then experience a second decay (ν_2) to the 1S level. The combined energy of the two transitions will be equal to the transition energy of a Lyman α transition ($\nu_1 + \nu_2 = \nu_{Ly\alpha}$).

The two-photon radiation process gives rise to an emission coefficient

$$4\pi j_\nu(2\gamma) = n_{2^2S} \frac{h\nu}{\nu_{Ly\alpha}} A(y) \tag{3.27}$$

where

$$A(y) = 202.0s^{-1}(y(1-y)(1-[4y(1-y)]^{0.8}) + 0.88[y(1-y)]^{1.53}[4y(1-y)]^{0.8}) \tag{3.28}$$

and $y = \nu/\nu_{Ly\alpha}$. The coefficient in $A(y)$ being derived from the total radiative probability for the $2S \rightarrow 1S$ transition and the population of the 2S state by recombination processes.

3.2.3 Line Emission: spontaneous bound-bound transitions

Spontaneous transitions from one bound state to a lower bound state of an atom or ion give rise to line emissions that are an important feature of PN spectra. Line emissions give clues to the composition of the PN, as well as the plasma density and temperature. The population of electrons in each excited state is dependent on the electron temperature of the system and on the overall electron density. By observing the strengths of each line relative to others in the same atom, we can derive the relative populations.

The Hydrogen and Helium Atoms

The hydrogen atom is modeled as a multi-level atom in the Cloudy case. Typically 50 levels are sufficient for accurate results. For the most part, the l-levels are considered to be "well-mixed" which means that the set of l-levels for any given quantum number n, are not considered as separate levels. The interactions with each n-level are considered to be one entity with some average of transition probabilities to all l-levels.

The exception is the n=2 level which is a special case. The 2S and 2P states are treated as separate levels to account for the uniqueness of the 2S level, which is noted in Section 3.2.2. It is important that both two-photon emission and collisional effects be properly calculated for this level.

The helium ion and the neutral singlet state are each treated as a 10-level atom in Cloudy completely analogous with the hydrogen atom with full l-mixing with the exception of the n=2 level. The neutral helium triplet states are slightly more complex. Special attention is paid to the 2^3S metastable state by including transitions from the singlet state.

Heavier Elements

It is sufficient and convenient to describe the most important forbidden line emissions by using a five-level atom as described in Section 2.7. The two basic electron configurations are shown in Figure 2.2. While the ground state configurations of atoms will be different, the energy structure of the first few levels immediately above the ground state have the same configuration. Note that Cloudy results will be less accurate at higher temperatures and densities where the higher excited states of the heavier elements will play a more important role. This is not a concern with the current models presented in this work.

Emission Coefficient

The emission coefficient for spontaneous line emissions from an upper level i and lower level j is given by:

$$4\pi j_{\nu}(i,j) = n_i A_{i,j} h\nu_{i,j} P_{ij}(\tau_{ij})\epsilon \tag{3.29}$$

where $A_{i,j}$ is the Einstein coefficient, P_{ij} is the net escape probability, n_i is the population density of the upper level and ϵ is the filling factor.

The level population density n_i is found using the statistical equilibrium equation, which balances all electrons entering the level via collisions and those leaving the level via collisions and spontaneous decays, as well as an assumed T_e and n_e which is derived for each layer in Cloudy during each iteration.

For resonance transitions (strong permitted transitions to the ground state) such as Lyα transitions of hydrogen and helium, the escape probability is of the form

$$P_l(\tau) = (1 + b(\tau)\tau)^{-1} \tag{3.30}$$

where $b(\tau)$ is tabulated.

For permitted lines of higher excited states, the escape probability (at depth τ

from the illuminated face) takes on the form:

$$P_{i,j}(\tau, T, X_c) = \{1 - X_c F(X_c)\}\frac{1}{2}\{K_2(\tau, X_c) + K_2(T - \tau, X_c)\} \tag{3.31}$$

where X_c is the probability of the line being absorbed into the thermal continuum and $F(X_c)$ is a function of the line shape. $K_2(\tau, X_c)$ is a function describing the opacity towards the front and back faces given depth τ of the emission. The above functions are described by Ferland (1997).

For forbidden line transitions, the escape probability is assumed to be unity as they are assumed to be optically thin.

3.2.4 Dust Grains

Dust grains are not included by default in the Cloudy program, but any number of types of dust grains can be added to the model. The code will consider the radiative and collisional heating and cooling of the grains.

In grains, the processes analogous to photoionization and recombination in atoms are the photoelectric effect and collisional charging. The photoelectric effect depends on the grain potential, which describes the energy required to pull an electron away from the grain. The grain potential is explicitly calculated through charge balance and establishes the critical energy required to ionize the grain. Cloudy uses a "sticking probability" S to calculate the likelihood that an electron will stick to the grain during a collision. For positive ions and neutral particles, S is the energy transfer efficiency and the accommodation coefficient respectively. S is generally set to unity.

Dust grains will gain energy by absorbing the surrounding radiation at wavelengths above the critical value. Below the critical wavelength, electrons can escape and some energy will be lost in the process to those electrons. Collisions between the grains and the electrons, ions and neutral particles result in further heating of grains (and thus, cooling of the gas). Grains will gain energy through kinetic and chemical interactions while also allowing for changes in the grain potential and thermal grain effects resulting from the collisions.

The grains radiate naturally producing a cooling effect which is defined by:

$$\Lambda = \int_0^\infty Q_\nu \pi a^2 n_d B_\nu(T_d) d\nu. \tag{3.32}$$

A grain temperature is derived by balancing the grain heating and cooling effects. The program will check that grain sublimation temperatures were never reached during the modeling procedure thus ensuring the survival of the asserted grains. A warning will be printed if the calculated grain temperatures exceeded 90% of the sublimation point at any time.

3.2.5 Input Parameters for Cloudy

The primary input file for Cloudy is a text file containing the assumed stellar parameters, the nebular characteristics desired and optional dust component characteristics which were used in both our models.

Stellar Parameters

The central source of the PN model must be defined with the model radiation field (Section 3.2.2), temperature (Section 2.5), luminosity (Section 2.3) and possibly a chemical abundance. Stellar parameters are based on current observational parameters whenever possible. For chemical abundances we default to standard solar values when reliable observations have not been made.

Nebular Parameters

The inner radius of the ionized region must be defined. It is optional to include an outer radius. We fit the outer radius by evaluating the outer radius achieved with each model created. Since the ionization front is not necessarily at the outer radius of the nebula, attention needs to be paid to the 50% ionization radius value in the diagnostic output file, where the ionization is rapidly decreasing to neutrality.

Cloudy allows for the nebular model to be open or closed and static or expanding. We assume a spherical geometry which is closed and expanding. The closed geometry creates an environment where the radiation leaving the side facing the source will be absorbed by the other side of the nebula. For an open geometry, that radiation will leave the system. An expanding geometry will satisfy case B predictions but the diffuse line photons will not interact throughout the nebula. A static nebula assumes the shell is stationary and includes the interactions with diffuse line photons.

The hydrogen density within the ionized region is specified as an input parameter and estimated values are taken from current observations whenever possible. It can be either constant across the nebula, as in NGC 7027, or a density distribution can be explicitly stated in the primary input file, as is the case for IC 418. Depending on the format chosen, the values (up to 500 pairs) for hydrogen density and its position from the center are entered as a list in either decimal or log values. Linear interpolation of intermediate points is done by Cloudy.

The filling factor ϵ, described in Section 2.2.1, is set to unity for the initial model. Once the model $F_{H\beta}$ is acceptable, the value is decreased to fit the outer radius of the nebula.

Dust Grains

Any number of dust grains can be added to the system. The primary input file contains the dust abundance, an index number to identify the grain and the name of a data file containing the associated wavelength-opacity grid, if required. A constant dust-to-gas mass ratio is assumed throughout the system. The abundance is quoted as a scaling factor to the standard nominal dust-to-gas mass ratio (see Section A.3) which is applied to the opacity grid during computations. Cloudy contains default grain opacity information for a collection of commonly used sets of dust grains (standard ISM, Orion nebula...) which then only requires an abundance and the number associated to the default dust grains. Our models do not use the defaults but instead supply the wavelength-opacity grid derived from the Mie Theory directly for the given type and size of grain as discussed in Section 3.1. The input data file to Cloudy contains the photon energy (in Ryd, see Appendix A.2.1) and the absorption and scattering cross-sections per hydrogen atom for the given dust grain.

Sample Input File

```
Title Model for NGC 7027
hydrogenic levels 50
blackbody 198100.0 K
# This is from Latter et al. (2000), H+ Zanstra temperature
luminosity 3.946310349 solar
# total luminosity 8837.112 solar
filling factor 0.606
radius -1.899251921 parsecs
# rin = 0.01261 pc
# try to match a 50% H ionization radius of 0.02069 pc
sphere
hden 4.778151250
# H density 60000 per cc
abundances He -0.975 Li -8.69 Be -10.58 B -9.12 C -3.347 N -3.796 O -3.387
```

```
continue F -7.52 Ne -3.96 Na -5.96 Mg -4.66 Al -6.22 Si -5.21 P -5.32
continue S -5.03 Cl -6.96 Ar -5.72 K -7.29 Ca -6.05 Sc -9.11 Ti -8.47
continue V -9.49 Cr -7.83 Mn -7.80 Fe -6.00 Co -8.59 Ni -7.27 Cu -9.24
continue Zn -8.86
# The above are from Jeronimo Salas, or solar
grains -0.6 9 qheat
grains -0.3 10 qheat
grains -3.9 15 "amc0p075.opac"
print faint -6.0
punch lines,array last file="smd05_nf.lines"
punch element hydrogen last file="smd05_nf.hydrogen"
punch physical last file="smd05_nf.physical"
punch continuum last file="smd05_nf.continuum"
punch radio last file="smd05_nf.radio"
stop temperature 2000.0
```

3.3 Modeling the Dust Shell

The neutral dust shell portion of the nebula is modeled with DUSTCD by Leung. In this program, the shell is again divided into layers, which are treated independently then summed together at each iteration to create the whole radiation field emitted at each location. This is compared to and must balance with the total heating of the dust shell at a given dust temperature for each layer.

The central star provides the input energy to the ionized region while the output from the ionized region serves as the input radiation field to the neutral region. Both programs assume spherical symmetry and a constant dust-to-gas mass ratio in the region being modeled.

3.3.1 Energy Balance Equations

Cooling is given by:

$$\Lambda = \int_0^\infty Q_\nu \pi a^2 n_d B_\nu(T_d) d\nu \tag{3.33}$$

where Q_ν is the absorption efficiency of the grain which is set to unity if the dust grain radius is much larger than the photon wavelength. Otherwise, it is calculated by the Mie Theory (See Section 3.1.1) for a given type and size of dust grain. The Mie Theory results for each dust grain used has been calculated via a program written by Kevin Volk. B_ν is the standard blackbody curve at temperature T_d. Therefore, the cooling rate for the dust is a quantity that can be calculated assuming a dust temperature.

Heating of the dust is given by:

$$\Gamma = \int_0^\infty Q_\nu \pi a^2 n_d J_\nu d\nu \tag{3.34}$$

where J_ν is the mean intensity of the radiation field from the sum of the emergent radiation field from the ionized region and each of the layers of the shell, $J_\nu(r_i)$. The local radiation field, $J_\nu(r_i)$, is calculated for each layer during each iteration using an assumed dust temperature which is also used to calculate the cooling rate of the dust. If the energy is not balanced, then a new dust temperature will be used to recalculate the heating. DUSTCD will iterate in this way until energy balance is achieved with consistent dust temperature and $J_\nu(r_i)$ values.

3.3.2 Local Radiation Field

By using the radiation transfer equation, a value for the mean intensity of the local radiation field, J_ν can be found within each layer.

$$J_\nu = \frac{\int I_\nu d\omega}{\int d\omega} \tag{3.35}$$

$$= \frac{1}{4\pi}\int I_\nu d\omega. \tag{3.36}$$

DUSTCD explicitly calculates the intensity, I_ν, with the radiative transfer equation in order to find the mean intensity of the radiation field.

The radiation transfer equation describes the change in ray intensity I_ν as it passes through some medium. The equation takes into account both the energy added by the medium itself and the amount by which the incident ray is absorbed or scattered by the medium (the first and second terms respectively on the RHS of Equation 3.37).

$$\frac{dI_\nu}{ds} = \jmath_\nu - \kappa_\nu I_\nu \tag{3.37}$$

$$\frac{dI_\nu}{\kappa_\nu ds} = S_\nu - I_\nu \tag{3.38}$$

$$\frac{dI_\nu}{d\tau_\nu} = I_\nu - S_\nu \tag{3.39}$$

where $\jmath_\nu$ is the emission coefficient and κ_ν is the absorption coefficient. They describe the total energy emitted (or absorbed) per unit time per volume per solid angle. Dividing Equation 3.37 by κ_ν gives Equation 3.38. The following substitutions are then made to get Equation 3.39: $S_\nu \equiv \jmath_\nu/\kappa_\nu$ is the source function and optical depth is defined in Equation 2.13. s is the path length of the ray.

Using a ray tracing algorithm to solve for the intensity function, the local radiation field J_ν can be calculated from Equation 3.36.

3.3.3 Eddington Flux

The final step in DUSTCD is to create the output spectra for the system. This is done using the first moment of intensity, H_ν.

$$
\begin{aligned}
H_\nu &= \frac{\int I_\nu \cos\theta d\omega}{\int d\omega} \\
&= \frac{F_\nu}{4\pi}.
\end{aligned}
$$

Here, F_ν is called the Eddington Flux. This is the output from DUSTCD which is also calculated using the specific intensity found with the radiative transfer equation.

3.3.4 Input Parameters

The primary input file to the DUSTCD program defines the dust shell being modeled including the dust opacity array, the total optical depth at a reference wavelength, the stellar temperature and luminosity, and the inner and outer radii of the shell. A first approximation for the temperature profile and a dust density distribution are also included. The latter can be an indicator to read from a separate input file for more complex dust density distributions than what can be described by the primary input file. A temperature distribution can also be specified if desired.

The default heat source for the model is a blackbody at the centre of the dust shell based on the stellar parameters outlined in the primary input file. *pnspect.in* is a file which provides an alternate input radiation field. The file contains a pre-defined wavelength grid and values for the input spectrum ($F_\nu/4\pi$) normalized to 1 $L_\odot$ at a distance of 1 kpc. For these models, the input radiation field will be the emergent field from the ionized region as calculated by the Cloudy program and the default will be overridden by *pnspect.in*. Note that the output from Cloudy is at higher wavelength resolution than DUSTCD expects, so the data file must be rebinned to the wavelength grid defined in the latter program.

The input dust opacity grid is created with the same process as described in Section 3.1. The output file created when the features have been added has a wavelength grid formatted for input to DUSTCD. The input file contains the total optical depth expected for a pre-defined reference wavelength. The program will scale the input opacity curve to this reference value.

rhodust.in describes the dust density distribution for the neutral region (if an input file is required). The file contains the appropriate radius grid and the dust density values which are meant to be in cm^{-3} for the actual dust contribution. DUSTCD will scale the actual values to be consistent with the total optical depth (at a reference wavelength) as set in the primary input file. It will be the general shape of the density profile that is defined by this file.

3.4 Output Spectrum

In order to produce a complete output spectrum, the line and continuum information produced by Cloudy must be merged with the continuum output created by DUSTCD. The output from the two programs, however, have different wavelength grids. It is necessary to interpolate the continuum output by taking the difference between the input radiation field and the output continuum. The difference establishes a transformation curve which DUSTCD has essentially applied to the input radiation field. The line emissions are produced by the ionized region (calculated with Cloudy) are added to the transformed continuum.

Chapter 4

Spectral Model for IC 418

IC 418 is a bright, compact, low-mass PN located at Galactic coordinates $l = 215.2°$ and $b = -24.2°$. The central star is the variable star HD 35914. The stellar temperature is low for a PN central star at ~40,000 K. The young PN is ~850 years old and still optically thick to ionizing radiation. It is a carbon-rich object with the C/O ratio estimated at 1.3 (Volk & Cohen 1990).

The PN has a fairly simple structure that is slightly elliptical in shape with a hollow cavity around the central star. Work by Louise *et al.* (1987), Monk *et al.* (1990) and Phillips *et al.* (1990) provide observations that reveal not only a highly ionized region bright in the optical with radius $6''$ but also an extended ionized region out to $20''$. A strong infrared excess suggests that there is a significant dust component in the ionized region of the nebula. Figure 4.1 shows an image of IC 418 taken with the Hubble Space Telescope (HST) through a [NII] filter on the left (Fig. 4.1a) and through an [OIII] filter on the right (Fig. 4.1b). The central star is in the middle of a nearly spherical nebula and the bright ring at $6''$ is seen as the darker outer region in Fig. 4.1a. In Figure 4.1b, the darker features surrounding the central star highlight [OIII] emission which requires higher temperatures. However, the infrared excess confirms the presence of dust in the nebula. The remaining ionized region out to $20''$ does not radiate brightly and is not shown in either image.

A neutral halo has been detected by Taylor *et al.* (1989) but Hoare (1990) finds that the halo has very low density and the emissions are only important at 100 μm

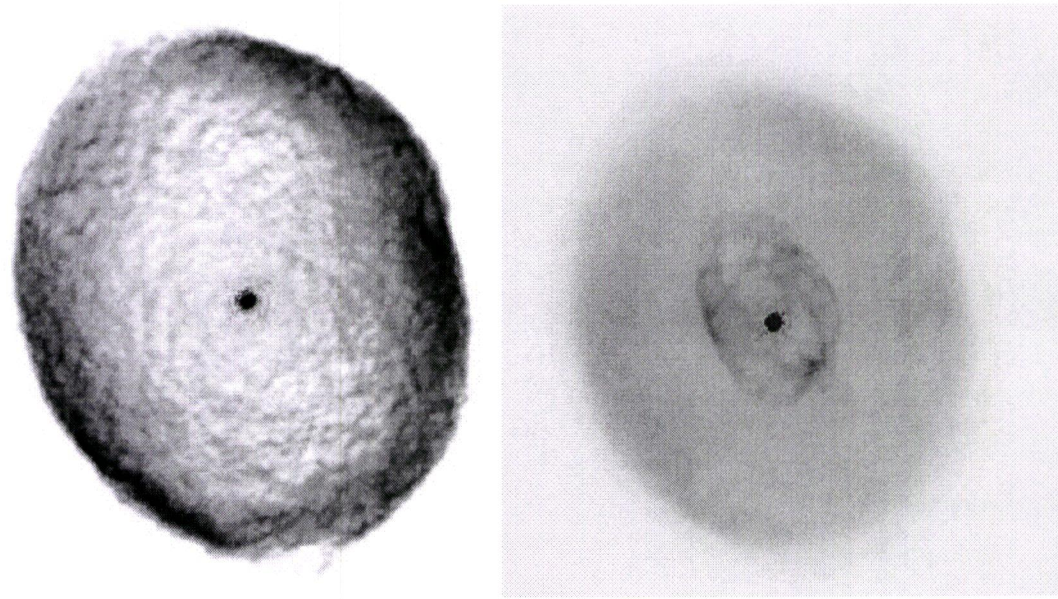

Figure 4.1: IC 418 as seen by the HST. The image on the left is with the [NII] filter where the dark outer edge is at $6''$. The image on the right is through an [OIII] filter which shows emission closer to the central star. These two images are essentially to scale such that the [OIII] emissions fit into the dark ring in the [NII] image. A full colour image can be found at http://heritage.stsci.edu/public/2000sept7/ic418table.html. (This image was produced by J. Stoesz.)

which is beyond our wavelength range of interest.

The computer model for IC 418 was constructed with Cloudy alone to reproduce the extended ionized region. The model was constrained by the $H\beta$ flux, the 5 GHz flux, the stellar V magnitude and certain line diagnostics which will be presented in Section 4.3. The model spectrum has been compared to the ISO data, paying special attention to the underlying continuum longward of ~45 μm and near ~16 μmand the peaks near 27 and 30 μm (see Figure 4.3).

In Section 4.1, observed parameters will be presented that will form the basis of our model. Section 4.2, the final models will be presented and compared to the ISO data. The results include a discussion of the 11.3 μm feature which has generally been attributed to silicon carbide, but does not appear to be the case here. The comparisons to the constraining parameters and a discussion will follow in Section 4.3.

4.1 Parameters

The distance to IC 418 is an uncertain value ranging from a fairly unreliable value of 0.42 kpc by Pottasch (1984) to a Shklovsky distance of 1.8 kpc (Cahn and Kaler 1971). Barlow (1987) finds an upper limit of 1.4 kpc with O[III] line diagnostics. The commonly adopted value of 1.0 kpc (with an error of a factor of 2) is from Taylor & Pottasch (1987) who found the value by comparing total column density for HI in the line of sight to the integrated optical depth from an observed 21 cm absorption feature. This model uses a value of 1.1 kpc. This distance is a consequence of adopting the $6''$ radius from observations and an inner radius value of 0.032 pc from Henry, Kwitter & Bates (2000) (hereafter HKB 2000).

The structure of IC418 is slightly ellipsoidal with a small cavity at the center and a thin, high-density photoionized region at $6''$ from the central star. The nebula is ionized out to $20''$ and then a neutral halo extends out to $80''$. This basic structure is adopted from Meixner *et al.* (1996). The structure is modeled with spherical symmetry. A high-density region begins at $6''$ and is approximately $1.2''$ thick (from HKB 2000). An inverse-squared density distribution extends out to $80''$ with a shock discontinuity at the interface between the two regions. The density drops by a factor of 4 at the discontinuity as a result of the adiabatic outward facing shock as described by the ISW model (see Section 1.1).

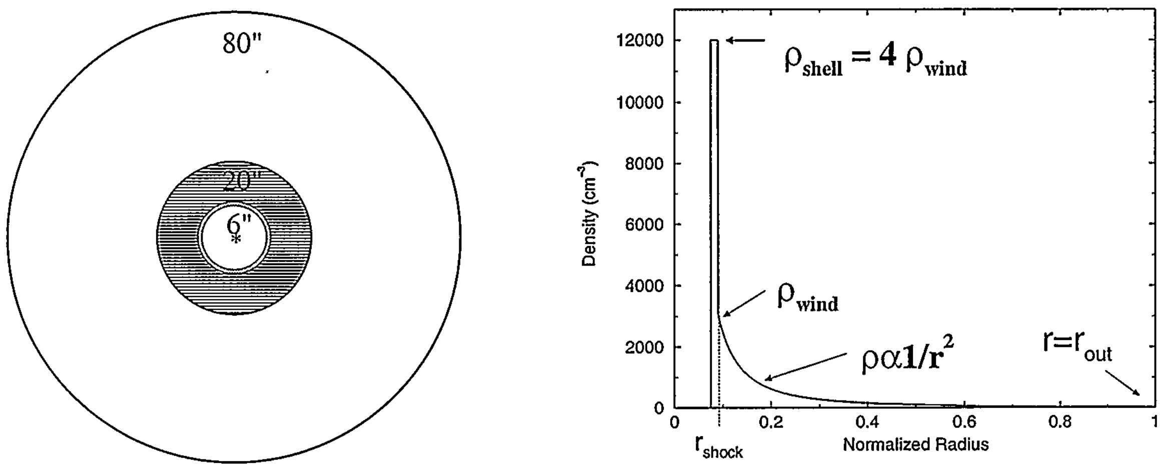

Figure 4.2: Basic model structure of IC 418. On the left, the solid shaded area at $6''$ is the thin, high-density shell and the line-shaded area indicates the extent of the ionized region. The wind region is solid white. The density distribution for the model is shown on the right.

The central star temperature is ~40,000 K. The initial 38,000 K blackbody model adopted (as per HKB 2000) could not reproduce the observed outer radius and $F_{H\beta}$. A 41,000K (g = 1000 m/s^2) Kurucz model (see Figure 3.1) was used to achieve a better fit. A discussion on the issues will be presented along with the base model results in Section 4.2.1.

The luminosity used was 3200 $L_\odot$. This value was adjusted to achieve a good fit to the $H\beta$ flux and stellar V magnitude. This is also consistent with stellar theory for a central star similar to that of IC418 (Hoare 1990).

Abundances are from HKB 2000 or are solar. Extinction is derived from the $\frac{H\alpha}{H\beta}$ ratio for a c-value of 0.14 ($E(B-V) = 0.1$ magnitudes or $A_V = 0.3$) which is also from HKB 2000.

Hoare (1990) used both a SiC and graphite mix and a SiC and amorphous carbon mix. He concluded that the SiC+AmC mix is a better fit with the graphite mix giving too flat a continuum. Following Hoare (1990) and Meixner *et al.* (1996), this model uses an amorphous carbon based dust continuum.

4.2 Model Results

Three models will be presented for IC 418. The base model is the model used to establish the underlying dust continuum with no added dust features of any kind. Model A contains only AmC grains with the 21, 27 and 33 μm features while Model B contains SiC grains in addition to the dust established by Model A.

4.2.1 Base Model

A base dust continuum model was created before any dust features were added to the system. The continuum was intended to match the ISO data between 13 and 20 microns and again longward of 50 microns. In Figure 4.3 the base continuum model is shown to satisfy the criteria. The $H\beta$ flux of 3.58×10^{-13} W/m^2 and the stellar V magnitude are good fits to observations (see Section 4.3). The main variables at this stage were the dust grain radius and the abundance.

The base model contains a 0.05 μm AmC dust grain with a dust-to-gas mass ratio of 1.2×10^{-3}.

In order to achieve this model, there were significant problems fitting the physical constraints of the nebula. The early models used a gas density of 2138 cm^{-3} derived from observed optical line ratios for the model. These models were density bounded (there were plenty of ionizing photons left after the entire nebula was ion-

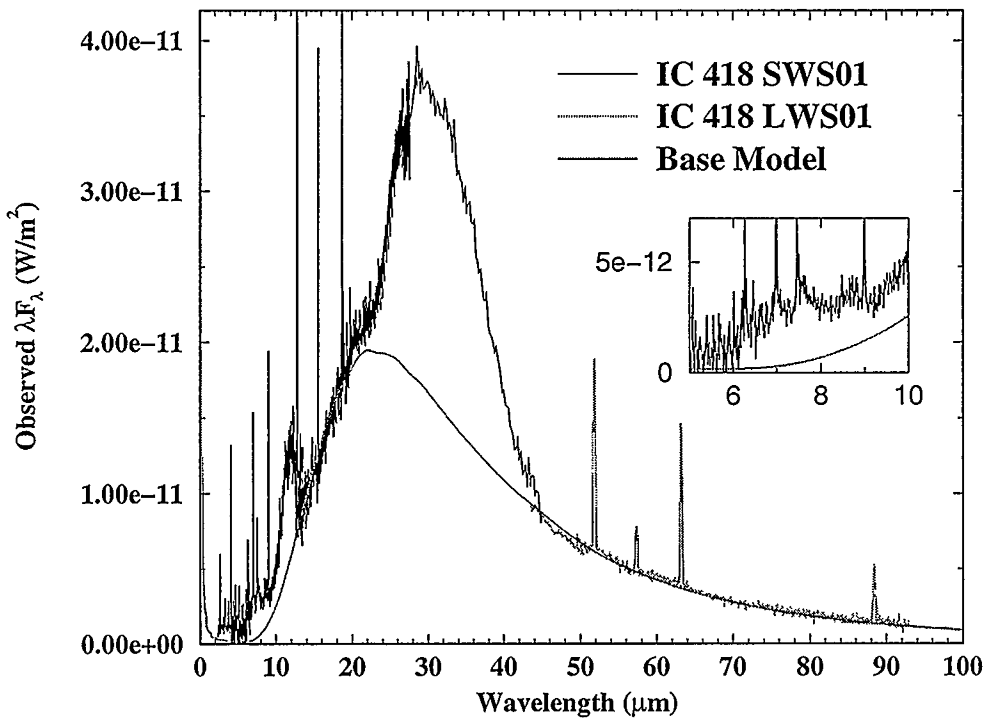

Figure 4.3: IC 418 Base Model with a 0.05 μm radius AmC dust grain and no features. PAH features observed between 7 and 9 μm are shown in the inset image.

ized), therefore we adopted the input density value of 12,200 cm^{-3} (HKB 2000). The degree of ionization continued to be a problem with the blackbody model. Even at the new high density gas in the shell, the nebula could not be ionization bounded within the observed nebular radius. The model results had either too much $H\beta$ flux or an unreasonably large nebular radius. The Kurucz model was able to provide a reasonable fit to both the outer radius and the observed $H\beta$ flux.

Figure 4.3 shows the features which are present in IC 418 above and beyond the dust continuum. The most significant feature is at 30 μm with a second distinct feature at 11.3 μm. There is also a very weak feature near 20-21 μm. The features between 6 and 10 μm are highlighted as PAH features in the inset image.

The PAH grains were not explicitly added to the final model due to a discrepancy near 11.3 μm which will be discussed in the next section, but will be mentioned here for completeness. Models containing the PAH feature alone showed only the 7.7 and 8.8 μm features and and not the two features at 6.3 and 7.0 μm. Both features present had much lower flux than the ISO data which may be the result of poorly modeled quantum heating effects.

With a reasonable base model, the features will be added to create two models (A and B). The two models result from the fit (or lack thereof) of the SiC feature which has largely been assumed to be the carrier of the 11.3 μm feature. This will be discussed in Section 4.2.3 after a discussion on the 21, 27 and 33 μm features which are the main focus of the models.

4.2.2 Model A: no SiC grains present

The ionized region is modeled with 0.01 μm amorphous carbon dust grains with 21, 27 and 33 μm features at 0.20, 1.05 and 1.40 times the base continuum strength respectively. The filling factor (ϵ) was adjusted to a value of $\epsilon = 0.709$ to match the outer radius of the nebula at 0.107 pc ($20''$ at a distance of 1.1 kpc). Figure 4.4 shows the results for this model and Figure 4.5 shows the opacity function for the collective dust content.

Between 13.0 and 20.0 μm, the amorphous dust grains produce a continuum that is too low (flux is $\sim$14% lower than observed) to match the observed data. The original base model that produced a good fit to this region was modeled to a dust temperature of 130 K at the inner radius. Efforts to match observations better with a smaller dust grain improved the fit only up to the 0.01 μm radius that we settled

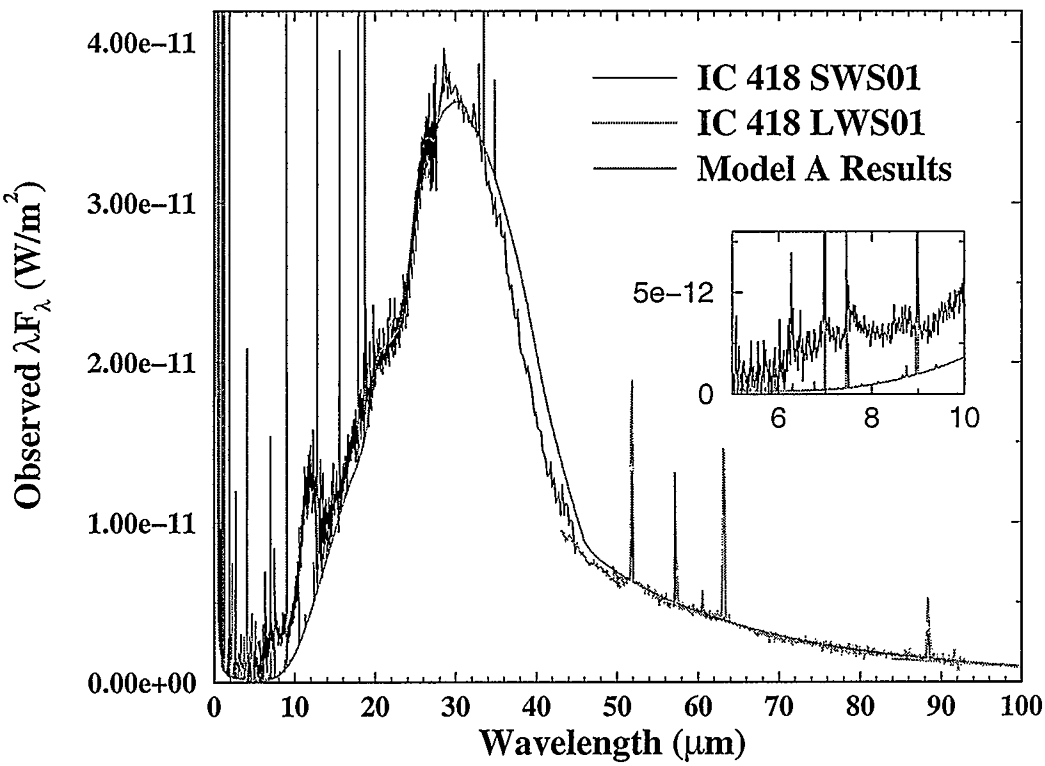

Figure 4.4: IC 418 Model A results. 0.01 μm radius AmC dust grains with 21, 27 and 33 μm features (see opacity curve in Fig. 4.5).

with in the final model with a dust temperature of 128 K.

The decrease in size is to accommodate the lower dust temperature that results from the addition of the opacity functions associated to the 21, 27 and 33 μm features. The opacity function resulting from the addition of the features produce more emission in the IR which is a cooling process not present in the original model. A smaller grain is needed to provide a hotter dust temperature similar to what was achieved with the base model. This was not unexpected in creating the base model without any additional dust features present.

As a result of the ill-fitted (but best fit) dust continuum, the 21 μm feature

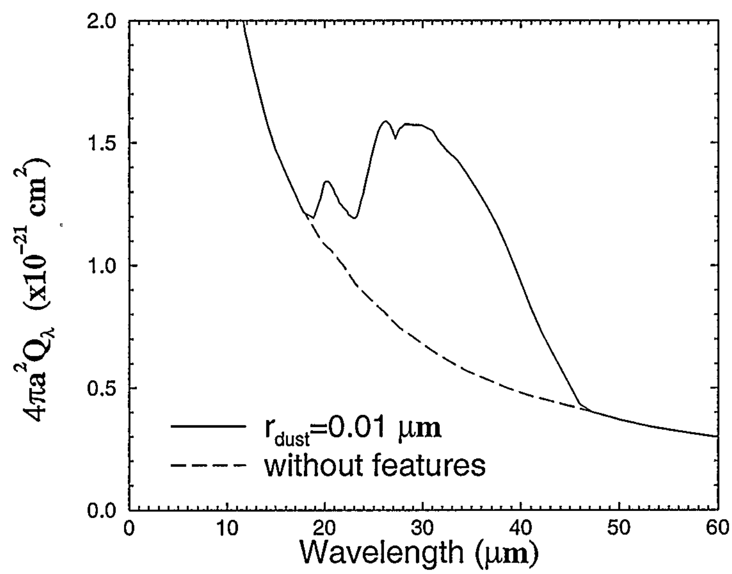

Figure 4.5: Feature strength profiles for IC 418 Model. 0.01 μm AmC dust grains with 21, 27 and 33 μm features

strength is most likely over-estimated in the final model presented here. It could be as weak as 0.1 times the continuum when applied to a more accurate model. A well-fitted continuum will have a shape like the base model in Figure 4.4, which would have an increased flux over the current model from the edge of the 11.3 μm feature ($\sim$13 μm) to the base model peak ($\sim$22 μm). Since the 21 μm feature sits in this region, it is reasonable to suspect that the current model feature would be too strong as a result. Therefore, while the feature is certainly present in IC 418, the strength should be taken with the proper perspective.

There is a peak observed at 29 μm that is most likely a result of bad data from ISO Bands 3E and 4 and not a true feature. The latter band is sensitive to cosmic ray hits which needed to be removed from the data. The selection of noisy points is subjective as it is done by eye rather than any analytical criteria. The remaining data points are subject to greater uncertainty in that range.

The model flux between 34 and 44 μm is approximately 23% higher than observed (Figure 4.4). This could be due to uncertainties in the ISO data, a result of the modeling assumptions made about the dust grains and the simplified physics in Cloudy, or a change in the 33 μm feature during the PN phase. The overall shape seems consistent with the observations, however, any change to the feature profile itself would be to become a narrower feature with the profile beginning closer to 40 μm.

4.2.3 Model B: SiC grains present

For Model B, two separate results are presented, both building on the established Model A. The first one (B.1) contains an abundance of 0.01 μm SiC grains necessary to match the peak flux of the observed feature near 11.3 μm. The second model (B.2, which will be representative of Model B in further discussions) contains a lower abundance of 0.01 μm SiC grains sufficient to match the observations along the short-wavelength side of the feature near 11.3 μm. The filling factor for Model B.1 is $\epsilon = 0.719$ and for Model B.2 is $\epsilon = 0.725$. The two models are compared with the base model and the ISO data in Figure 4.6.

While current models including those by Hoare (1990), Meixner *et al.* (1996) and Hyung and Aller (1994) indicate the presence of SiC grains, we find that they are not a sufficient match to the dust feature that peaks between 11.3 and 12.3 μm. A combination of SiC and PAH grains was also not sufficient to match the observed feature.

The first model will not be discussed in depth but it is clear from the results

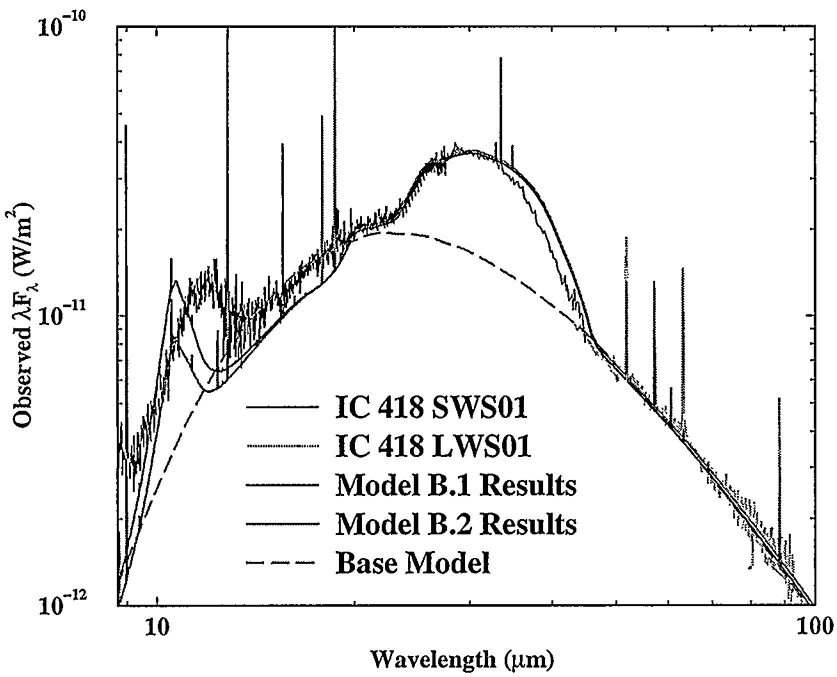

Figure 4.6: IC 418 Model B results. 0.01 μm SiC grains are added to Model A. Model B.1 matches the height of the observed SiC peak. Model B.2 is fitted to the observed continuum near 11.3 μm.

shown in Figure 4.6 that the SiC feature is a poor fit to observations. The observed feature is a wider feature than expected for SiC, but it is unclear whether it represents a single feature or a composite feature which includes a small SiC feature such as we have presented in Model B. We would like to extract a shape for the observed feature and a fitting procedure is therefore applied to both Models A and B to highlight either case. The Model A and B results are compared to the observed 11.3 μm feature in Figure 4.7.

The feature shape has been derived from each model and the observations, particularly the ISO-SWS data between 8.0 and 18.0 μm. First, the flux density from the observational data was divided by the model flux. A curve fitting procedure was

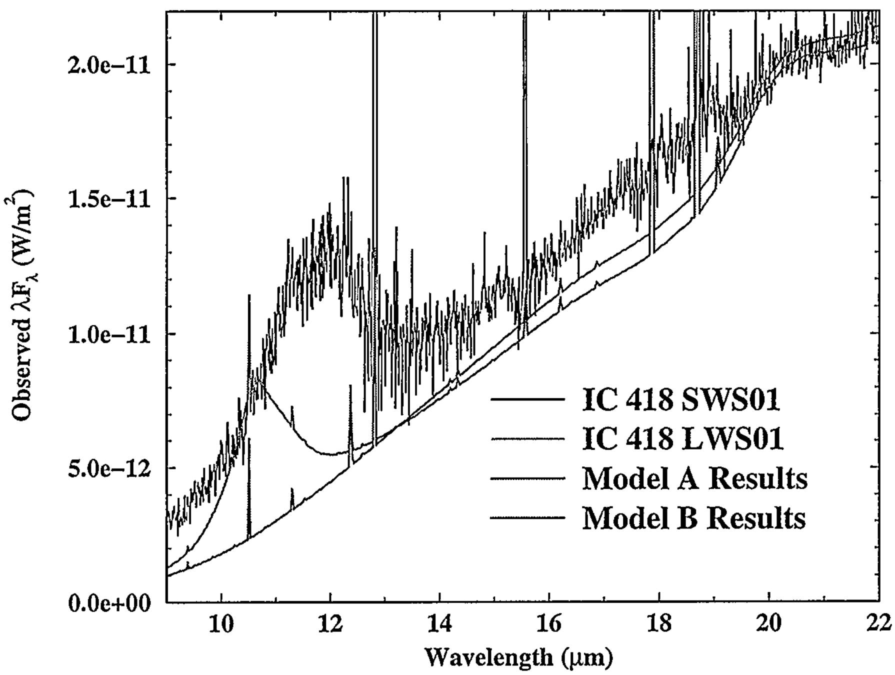

Figure 4.7: IC 418 Model A and B results zoomed on the 11.3 and 21 μm features.

performed to remove any portion of the continuum that was not fitted by the model and the result was subtracted to remove the underlying continuum completely. Finally, a second curve fitting was performed on the resultant relative opacity curve to determine a peak wavelength and feature width (FWHM). Before the final curve fitting, all strong line emissions were removed from the data and the data were trimmed shortward of $\lambda \approx 10$ μm. All curve fitting was done with a software package called TableCurve. TableCurve produced a list of possible fits. The best fit with respect to visual inspection and standard error was selected.

For Model A, shown in Figure 4.8, the best fit curve is a Gaussian with a peak at 11.4 μm and a FWHM of 2.13 μm. The feature appears largely symmetric but is wider than the observed SiC signature which was discussed in Section 1.8.

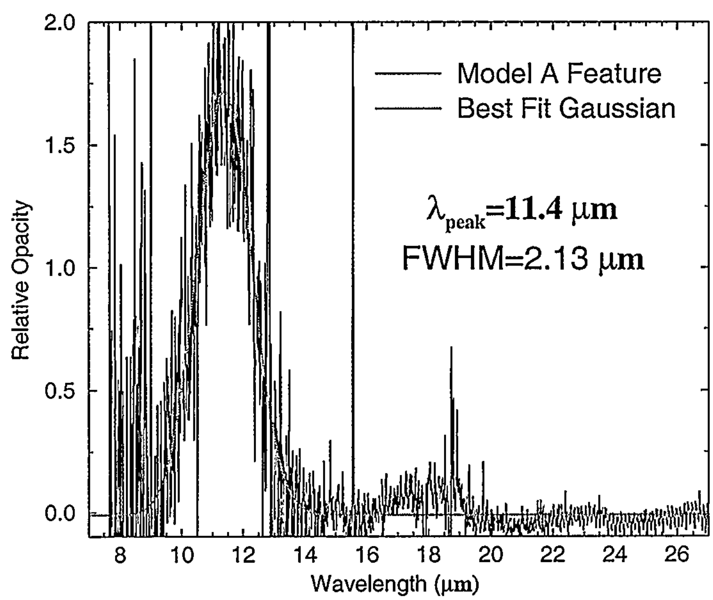

Figure 4.8: The "11.3" μm feature extracted from Model A.

For Model B, shown in Figure 4.9, the best fit curve is an "extra value" exponential to fit the more complicated curve resulting from the asymmetry of the extracted feature. The curve has a main peak at 12.0 μm and FWHM of 2.12 μm. The feature also has an extended tail towards the longer wavelengths.

In both derived features, there is what appears to be another feature between 16 and 19 μm. The excess in that region was removed from the data for the final curve-fitting procedure for Model B. The bump is not a feature but a result of the fitting procedure and the fit of the model to the observations. Figure 4.7 shows the difference in flux between the models and the observed data. The 21 μm feature begins at 18.8 μm where the fit becomes very good. In Figure 4.7, the relative opacity where the model fit with observations is approximately zero. This is true at

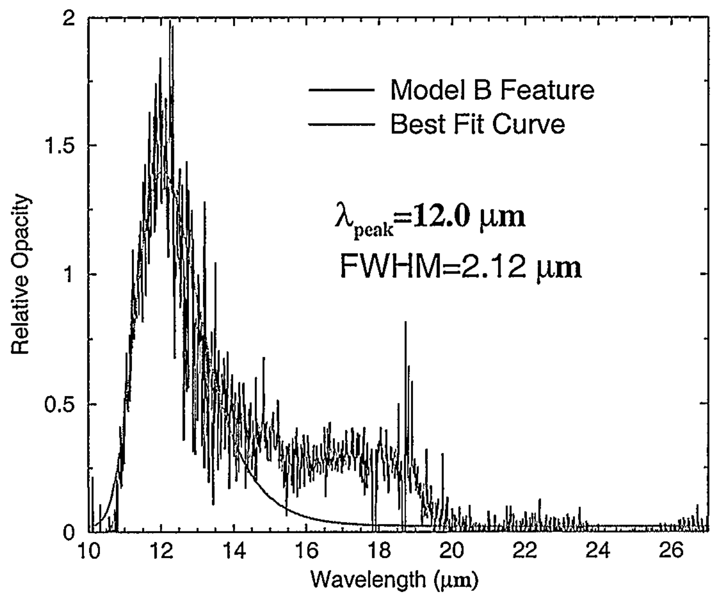

Figure 4.9: The 12.0 μm feature extracted from Model B.

wavelengths beyond 19 μm. Prior to that, the best fit dust continuum is not adequate to agree with observations (as discussed in Section 4.2.2). A linear fit was used to compensate for the ill-fitted flux density between 13 and 19 μm. This assumption may be responsible for the 16 to 19 μm bump that is seen in both extracted features presented here, since the models do not have a truly consistent linear flux density difference with the ISO data.

4.3 Analysis

The Model A $H\beta$ flux is 3.29×10^{-13} W/m^2 which is at the lower limit of the observed flux of $(3.47 \pm 0.18) \times 10^{-13}$ W/m^2 (the dereddened value from Acker *et al.* (1992)). The $H\beta$ flux for Model B is slightly lower at 3.27×10^{-13} W/m^2.

The model stellar V magnitude of 9.87 is consistent with the observed value of 10.17 which dereddens to 9.87 for the assumed A_v of 0.3 magnitudes.

As with Hoare (1990) and shown for our model in Table 4.1, there is not a good fit to the line ratios, the 5 GHz or the 15 GHz flux densities. This is a problem encountered by all the models referenced by this work and needs to be addressed in order to improve the model results in general. The fit is adequate for our discussions on dust but should continue to be a concern in the future.

	Flux Density (Jy)	
Frequency	Observed	Model
4.885 GHz	1.613	1.0075
14.965 GHz	1.529	0.8949

Table 4.1: Observed and Model Flux Densities for IC 418. Observed values from Acker *et al.* (1992)

The dust-to-gas mass ratio for amorphous carbon is derived as 1.6×10^{-3} in the ionized region (see Section A.3). Hoare (1990) found 6×10^{-4} with a factor of 3 error for AmC. Pottasch *et al.* (1984) found 2.4×10^{-3} for a model with a single grain size instead of the distribution used by Hoare. This model is more consistent with our single-grain size model and the resulting dust-to-gas mass ratio is also consistent with ours.

From Model A, the electron temperature is derived as 11,300 K and 11,000 K from model [NII] and [OIII] line ratios respectively. The model electron density is 3440 cm^{-3} and 3411 cm^{-3} from the [OII] and [SII] pairs. These values are consistent with HKB 2000, although they found the temperature for the region containing singly ionized atoms to be slightly lower than the temperature containing doubly ionized material. Our temperatures (representing singly and doubly ionized regions) are similar to each other and within error of their values.

	Zanstra Temperatures (K)	
	Model	Observed
Hydrogen	36100	36000
Helium I	35700	–

Table 4.2: Model Zanstra Temperatures for IC 418. The observed value is from Pottasch (1984)

The Zanstra temperatures derived from our model results are consistent with Pottasch (1984) (which is noted in Table 4.2), Hoare (1990) and HKB 2000. The similarity between the hydrogen and helium Zanstra temperatures indicate that IC418 is indeed optically thick.

Table 4.3 shows a comparison of line ratios derived from our model, a number of model values presented by HKB 2000, and observed values presented therein. Line headings in Column 1 that contain only one line are taken with respect to $H\beta$=1.

Flux seems to be in general about 50% lower than observed. The general line ratios between lines from the same atom are consistent with observations but the line ratios compared to the $H\beta$ are low. This suggests that the chemical abundance model is not adequate, but does not affect the discussion of these results. Changes in the abundance will affect the line intensities but not the dust continuum to any appreciable amount and will therefore not greatly affect the model results achieved here.

Lines	Line Ratios			
	Observed (HKB)	Model(HKB)	Model A	
4363/5007	4.0738(-3)	7.762(-3)	8.837(-3)	[OIII]/[OIII]
6717/6730	0.6026	0.4898	0.6674	[SII] / [SII]
6584/3727	1.51	1.58	1.57	[NII] / [OII]
1909/5007	0.229	0.282	1.14	CIII] / [OIII]
5755/5007	3.252(-2)		3.257(-2)	[NII] / [OIII]
5007/3727	1.0*		1.2	[OIII] / [OII]
1909	0.28		0.68	CIII]
3727	1.15		0.54	[OII]
4363	5.0(-3)		5.31(-3)	[OIII]
4959	0.36		0.21	[OIII]
5007	1.23		0.60	[OIII]
5755	4(-2)		1.96(-2)	[NII]
6584	1.75		0.842	[NII]
6563	2.86		2.87	$H\alpha$
6716	3(-2)		0.118	[SII]
6731	5(-2)		0.177	[SII]

Table 4.3: Observed and Model Line Ratios for IC 418. From HKB 2000 except * which is from Mendez *et al.* (1988).

4.4 Summary

The model for IC 418 presented in this work is consistent with previous work as cited throughout this chapter. The final model is found to have the 21, 27 and 33 μm features present with a baseline 0.01 μm amorphous carbon grain. This serves as one of the first confirmations of the 21 μm feature in a PN which will be further discussed in Chapter 6.

The model spectrum profile is a good overall fit with the ISO data. This suggests that the PN is well-modeled by the assumption of spherical symmetry. The results are modeled by Cloudy alone which suggests that the primary emissions from the nebula out to 100 μm are consistent with the assumption that they originate from the ionized region alone. The fit to radio flux densities is problematic. It is uncertain what causes the poor fit, but the problem has been encountered by other current models.

Four main inconsistencies in the fit to observations are presented from the results. First, and to a lesser degree of concern, the line ratios are not well modeled which is largely a result of the nebular abundances. Our results are consistent with those presented by HKB 2000 who originally derived the abundances from observations. The line strength fits are not the focus of our models and will not affect our results significantly. However, this should remain a concern for future models.

IC 418 is a cool central star which is not well approximated by a blackbody as has been shown by our model and many previous. The choice of the stellar atmosphere model has been uncertain in recent models, with no single model providing a very good fit. So long as the key observational constraints evaluating the models were reasonably met, the stellar atmosphere model was accepted. This is also the case for our model which is consistent with previous work under the same limitations.

The base dust continuum falls short of the observed spectrum by ~14% between ~13 and 19 μm, which is attributed to the limitations of the Cloudy program in modeling dust in the ionized region.

The 11.3 μm feature which has generally been attributed to SiC is cast into doubt. The feature was not fit by a model SiC grain and it also does not appear to be consistent with a "dirty" SiC grain as presented by Borghesi *et al.* (1985). The feature near 11.3 μm was extracted from our models and shown to be wider overall than expected for SiC and to peak nearer 12 μm. More study of this feature is needed to identify the true carrier.

Finally, the density from the line diagnostics (observed and modeled) is smaller than the density used in the model for the high-density region (3400 cm^{-3} from the line diagnostics and 12,200 cm^{-3} in the high-density shell of the model). Since the ionized region is not at constant density, the line diagnostics are going to reflect some kind of average density across the entire region. The diagnostic lines in such cases must be used with caution and should only be used as a constraint for model fitting as opposed to a model value. This is another reason why the original low-density (2138 cm^{-3}) model was abandoned earlier in the project (see Section 4.2.1).

Chapter 5

Spectral Model for NGC 7027

NGC 7027 (central star HD 20122) is a young, hot PN at Galactic coordinates $l = 84.9°$ and $b = -0.4°$ that is emitting very brightly at all wavelengths. Calculations with wind velocities and nebular size place the nebula's age at ~600 years old. It is extremely carbon-rich with a C/O ratio of 3.1 (Volk & Cohen (1990)). The nebula contains hot and cold, atomic and molecular material making it ideal for many different studies of PN morphology.

The nebula's shape is much more asymmetric than IC 418. CO (Jaminet *et al.* (1991)) and molecular hydrogen (Latter *et al.* (2000)) emission maps both find evidence of jets along the major-axis of the bright central ionized ring. Observations show a central star with a bright, elliptical ring surrounded by a clumpy, asymmetric dust cloud. The structure can be seen in the HST image in Figure 5.1. HD 20122 is visible in the center of the bright ionized region through the clumpy dust which surrounds the nebula.

The computer model for NGC 7027 is therefore more complex than that for IC 418. The ionized region is modeled with Cloudy, then the external neutral region will be modeled with DUSTCD. The model will be constrained by a similar set of parameters as IC 418 ($H\beta$ and 5 GHz flux, stellar V magnitude and selected line diagnostics). We are looking for an overall fit to the continuum from the UV out to 100 μm, paying particular attention to the region between 15 and 35 μm.

The model parameters will be presented in Section 5.1 and the results in Sec-

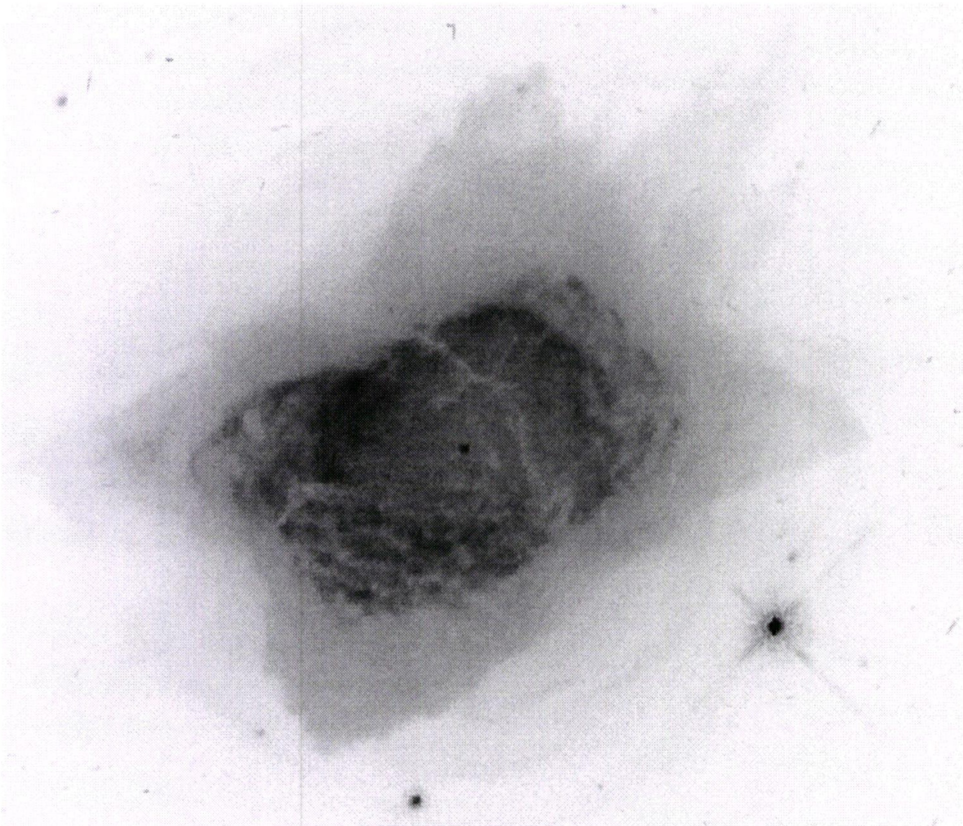

Figure 5.1: NGC 7027 as seen from Hubble. The ionized region is the dark oval with major-axis oriented along the bottom left - top right corners. The top portion of the ring structure is most visible. There are jets from the ionized region most prominently on the left central side. The ionized region is shrouded by a cloud of material which take on a nearly rectangular shape oriented along the major-axis of the ionized region. The central star is a black dot in the center. The full colour image from Ciardullo (1999) can be found at http://www.ucalgary.ca/~apei. (This image was produced by J. Stoesz.)

tion 5.2. The comparisons to observed data and a discussion will follow in Section 5.3.

5.1 Parameters

The distance is assumed to be 930 pc following Volk & Kwok (1997), and is consistent with those found by Masson (1986 and 1989) of 940 ± 200 pc and 880 ± 150 pc respectively. (See Section 2.6.)

NGC 7027 is a highly elliptical nebula with three distinct regions: an ionized region, a neutral high-density shell and a neutral wind region. The high-density shell has been observed by CO line emission (Jaminet *et al.* (1991) and Liu *et al.* (1996)). As a result of the computer programs assuming spherical symmetry, three separate models (discussed in Section 5.2), were constructed using three different sets of radii values. The basic structure of the model nebula is shown in Figure 5.2 with the observed major and minor-axes values of the ionized and neutral wind regions presented in Table 5.1 along with a set of average radii values. The high-density neutral shell in each case begins at the outer radius of the ionized region and has a thickness of $\sim 2.75 \times 10^{15}$ cm or 8.91×10^{-4} pc (0.2 arcsec at 0.93 kpc), which is consistent with models made by Volk & Kwok (1997) and Yan *et al.* (1999).

	Radius (pc)		
	min	average	max
r_{in}(ion)	0.009554	0.01261	0.01704
r_{out}(ion) = r_{in}(wind)	0.01758	0.02069	0.02795
r_{out}(wind)	0.1361	0.1602	0.2164

Table 5.1: Radius Values for NGC 7027 Models. The values assume a distance of 0.93 kpc to the nebula.

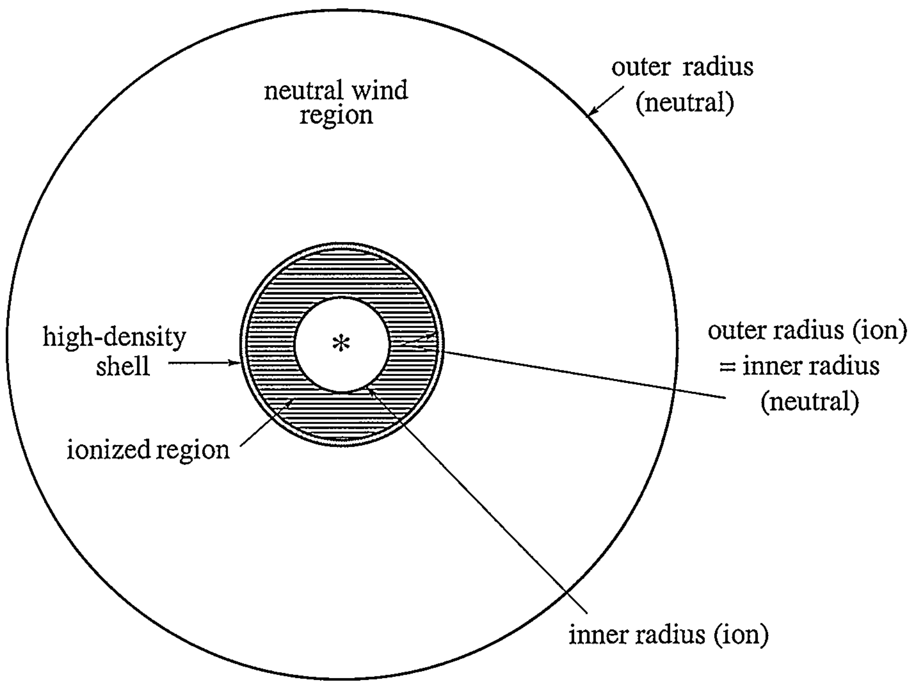

Figure 5.2: The structure of the NGC 7027 model is shown with the ionized region (striped), the high-density shell (shaded grey), and the neutral wind region (white).

The density of the ionized region is assumed to be constant at 60,000 cm^{-3} which is consistent with Roelfsema *et al.* (1991 and references therein) who derived a value of $(6.0 \pm 0.6) \times 10^4$ cm^{-3}. The exact density distribution of the neutral region (shell and wind regions) is not exactly known and various models will be discussed in Section 5.2.

Latter *et al.* (2000) used data from the Hubble Space Telescope (HST) and the Near Infrared Camera and Multi-Object Spectrometer (NICMOS) to image the molecular hydrogen in the nebula. They derived a hydrogen Zanstra temperature of $198,000 \pm 10,500$ K for the central star.

Luminosity was adjusted to satisfy the measured stellar V magnitude of 13.30 at the given distance of 0.93 kpc with the final model using $L_* = 8837\ L_\odot$.

Abundances are taken from Salas *et al.* (2001) or assumed to be solar.

Total extinction is calculated to be 3 magnitudes in total with ~1.2 from the ISM and ~1.8 from the circumstellar environment. We use E(B−V) = 0.315 for A_V of 0.972 for the ISM extinction. The extinction at wavelengths shorter than 0.25 μm is not a sufficient fit to the optical observations but this is not unexpected (see Section 2.4).

With observations in the millimetre and sub-millimetre wavelengths, Hoare *et al.* (1992) find evidence of warm and cool dust components surrounding the nebula. They suggest that the dust is "not significantly destroyed in the ionized region" since they find maximum dust-to-gas ratios of 7×10^{-4} and 1.5×10^{-3} for the ionized and neutral regions respectively. They use the observations to determine if the dust is amorphous or crystalline in nature by establishing the emissivity law $\epsilon \propto \lambda^{-\beta}$, where $\beta \approx 1$ implies amorphous grains and $\beta \approx 2$ would suggest crystalline grains. They tried both graphite and amorphous carbon grains and found the emissivity of graphite to be inconsistent with observations and chose to use AmC grains only and suggested an inverse-squared radial dust distribution. These parameters are adopted for our model.

5.2 Model Results

NGC 7027 is a much more complex nebula to model than is IC 418. The final model compared to the ISO observations will be presented first followed by a discussion of the various methods used to achieve this model.

The final model contains 0.075 μm AmC dust and PAH grains in the ionized region and 1.0 μm AmC dust in the neutral shell with 27 and 33 μm features at 0.2 and 0.3 times the continuum respectively. No 21 μm feature is found in the spectrum. The filling factor for the average model is $\epsilon = 0.606$. Figure 5.3 shows the results for the model. The final dust distribution and opacity function are shown in Figures 5.4 and 5.5, respectively.

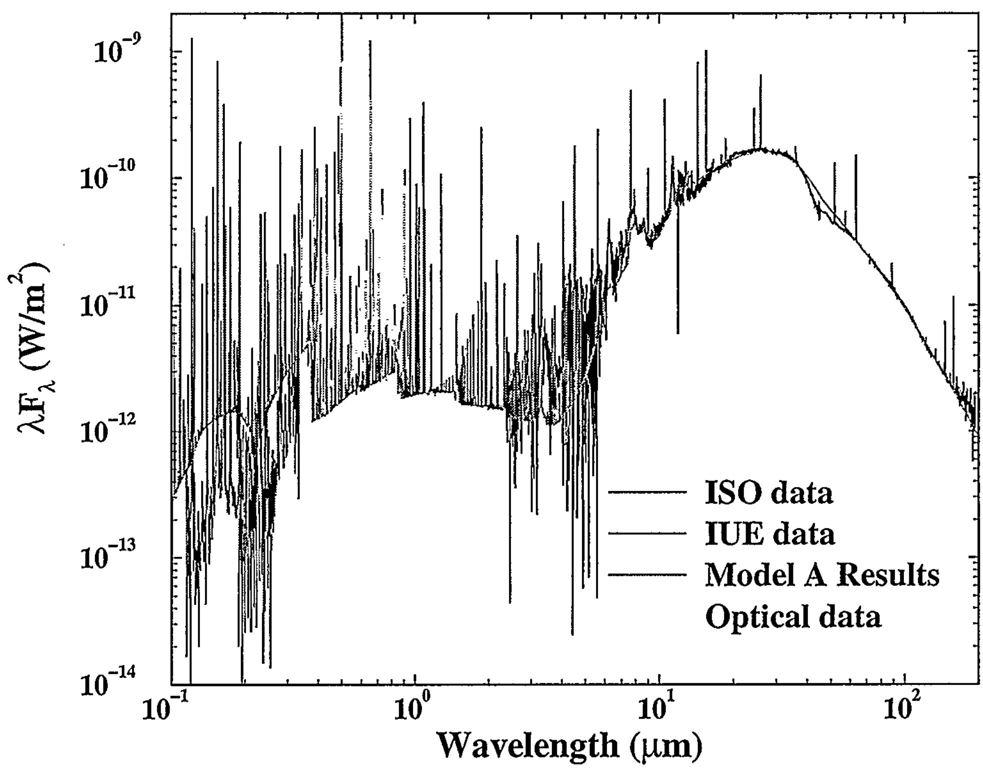

Figure 5.3: NGC 7027 Model A results. 0.075 μm AmC grains with no dust features in the ionized region. 1.0 μm AmC grains with features at 21, 27 and 33 μm in the neutral region.

The programs both assume spherical symmetry for the nebula, which is clearly not the case here. The main model has a radius that is the average of the semi-minor and semi-major axes values (see Table 5.1). The fit was not sufficient, so two additional models were created to approximate the elliptical structure of NGC 7027 better. The models are for a sphere with radial values equal to those of the semi-minor axis and for a sphere using semi-major axes values. The three models (semi-minor, semi-major and average radii) were averaged with equal weighting to achieve the final model results presented.

5.2.1 The Ionized Region

Initially, the nebula was modeled without any dust in the ionized region. The dust shell alone, however, was unable to fit the shorter wavelength continuum between 3.5 and 14.5 μm. A fit required hotter (or smaller) dust grains, which could not be achieved with the dust shell alone. A smaller dust grain with a radius of 0.075 μm was then added to the ionized region providing the best fit.

The model using the minor axis needs a larger filling factor (ϵ = 0.90) while the model using the major axis requires a smaller filling factor (ϵ = 0.25) in order to match the 50% ionization radius in either case. Observations have shown that the ellipsoidal shape of the nebula results from faster moving material expanding in the NE and SW directions. Our results would concur with the suggestion that this material expands faster due to lower density of gas and dust in those directions.

Two sizes of PAH grains are added to the ionized region: 0.001 and 0.00035 μm grains with the larger grains at half the abundance of the smaller ones. These grains are in keeping with Volk and Kwok (1997) based on Schutte *et al.* (1993). The best fit to the observations was made between 7.7 and 12.7 μm. The model PAH features at 3.3 and 6.2 μm are too small compared to observations. This indicates that the models are not adequately accounting for quantum heating effects. The PAH grains are not the focus of this study and are included to confirm their presence.

There is a bump or jump in the optical observations between 0.5 to 0.9 μm that is not fitted by the model. It is the extended red emission first seen in the Red Rectangle (Furton & Witt 1992) which is thought to be due to fluorescence in the unidentified IR (UIR) carrier molecule. It has not been included in our models.

5.2.2 The Dust Shell

The infrared spectrum longward of 45 μm and the basic shape of the peak between 20 and 30 μm were fitted first. Several density distributions were tested in the wind region: r^{-2}, $r^{-2.5}$, r^{-3} and $r^{-3.5}$. The inverse-square distribution was chosen as the best fit of these models.

There is a sharp bend in the observed spectrum near 45 μm. The early models produced spectra with transitions that were too smooth in that region. The fit to the bend was improved by increasing the density difference between the ionized region and the neutral shell. The model spectrum showed improved results with a density jump increased up to a factor of 100. No visible improvement was noted for jump discontinuities larger than that.

A good fit at wavelengths longer than 45 microns was still not achieved, with the dust never reaching adequately cool temperatures ($\leq$ 40 K). The wind region was then extended in order to reach a cooler dust temperature. Four models were attempted to test the hypothesis. The additional wind region beyond the outer wind radius model was extended out to 0.30 pc for each model or out to a radius of 1.87 $\times$ $r_{out}(wind)$ (which is the ratio taken for the average radius model). The extended region contains dust either with a constant density value which was reached at the outer radius of the wind region or continues the inverse-squared distribution. The best fit model was the constant density extension for all models out to 0.30 pc. This model fits the continuum between 20 and 35 μm and beyond 60 μm best but we are still unable to fit the sharp bend at 45 μm well.

In summary, the best fit dust shell model has a 1.0-μm AmC grain with a density drop of a factor of 100 between the high-density shell and the wind region. The wind region has an inverse-squared distribution out to the outer radius of the wind region then an additional constant density region (at the same density as the outer wind radius) out to a radius of 0.3 pc. The total opacity for the dust shell is τ ($\lambda =$ 11.22 μm) = 0.1004. This gives a dust particle density at the beginning of the wind region of $\rho_{wind} = 1.0 \times 10^{-10}$ cm^{-3} with the shell particle density being a factor of 100 larger.

5.2.3 21, 27 and 33 μm Features

Once the underlying continuum was fitted, the features were added to the opacity function for the dust with different strengths (see Equation 3.1. The best fit feature strengths are much weaker in NGC 7027 than in IC 418 at 0.2 times the continuum at 27 μm and 0.3 times at 33 μm (Figure 5.5) but still falls somewhat short of a perfect fit (Figure 5.7). No 21 μm feature is present in the model and would not appear to be present in the spectrum itself. Models with feature strengths as low as 0.02 times the continuum were made with the model feature remaining significantly larger than anything seen in the observed spectrum.

It is unclear whether or not the 27 and 33 μm features would be present in the ionized region. The model presented as the best fit model (Model A: Figure 5.3) does

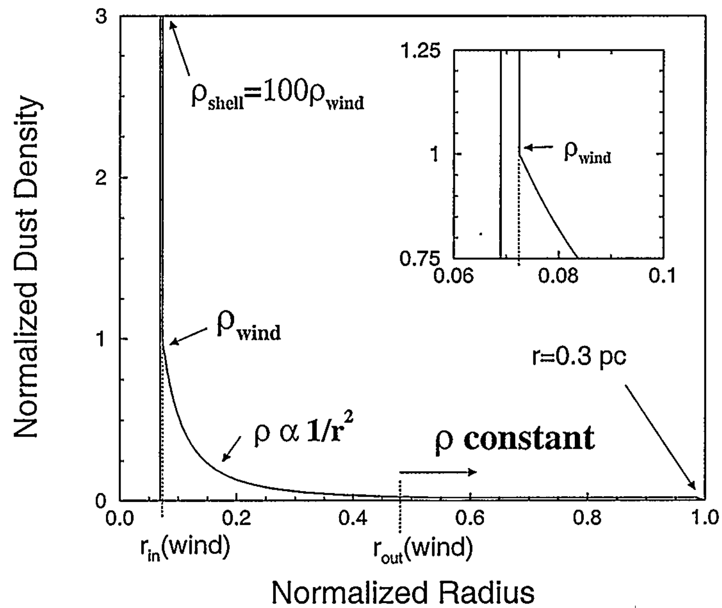

Figure 5.4: Dust distribution for wind region of NGC 7027. $r_{in}(wind)$ is the inner radius of the neutral region plus the thickness of the shell and $r_{out}(wind)$ is the outer radius of the neutral region (see Table 5.1).

not include any features in the ionized region. Figure 5.6 shows the model (Model B) which results from the inclusion of the features in the ionized region.

Figure 5.7 shows very little difference between the two models. However, there is a slight decrease in flux between 5 and 20 μm and a slight increase in flux around 23 to 40 μm. The increase at 30 μm appears to coincide with the weak feature in that wavelength range. However, with such weak features in NGC 7027, it is difficult to make any strong conclusions.

There is a good fit to observations between 15 and 40 μm and longward of $\sim$60 μm. The model was unable to reproduce the sharp bend between 40 and 60 μm despite various dust density distributions modeled. This could be a result of an evolution in shape of the 30 μm feature from the PPN to PN phases but is more

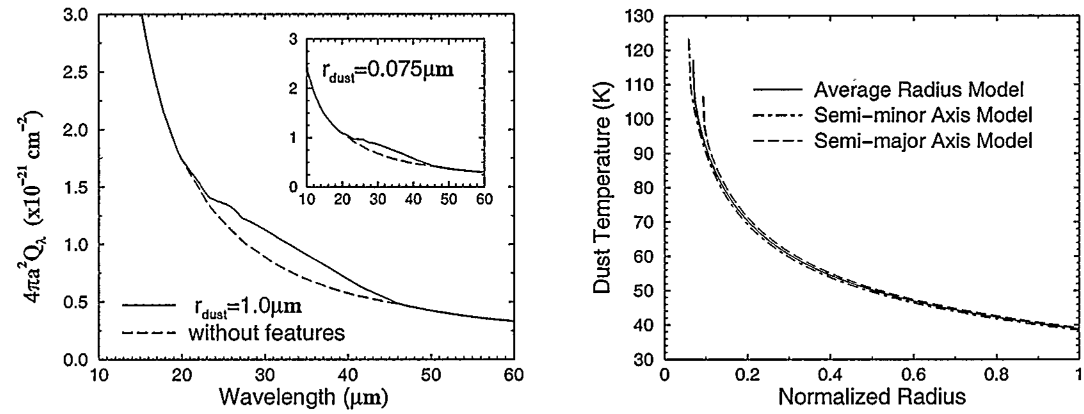

Figure 5.5: On the left is the opacity curve for the best fit dust component for NGC 7027 with the 27 μm feature and the 33 μm feature at 0.2 and 0.3 times the continuum. The resulting dust temperature profiles are shown on the left.

likely to be a problem with the dust modeling in the neutral region. In Figure 5.5, the 34 μm feature can be seen to begin at 45 μm. The model flux is already higher than observations between 45 and 58 μm. If the continuum were to model the observed curve better, the 34 μm feature would likely have a reasonable fit. There were considerable problems modeling the dust well in the neutral region, most likely as a result of the assumption of spherical symmetry which is an over-simplification of the observed nebular shape. The dust also has a non-uniform clumpy nature which can be seen in the HST image Figure 5.1. The final model reflects a best fit with the largest portion of the underlying continuum longward of 60 μm while maintaining the largest possible transition at 45 μm. Clearly, there are still significant problems with the simplified model.

If there is a change to the feature shape, the feature must be elongated towards the longer wavelengths as the carriers evolve. This is not what we see in the comparisons of the IC 418 model in Figure 4.4 which has much stronger feature strengths. There

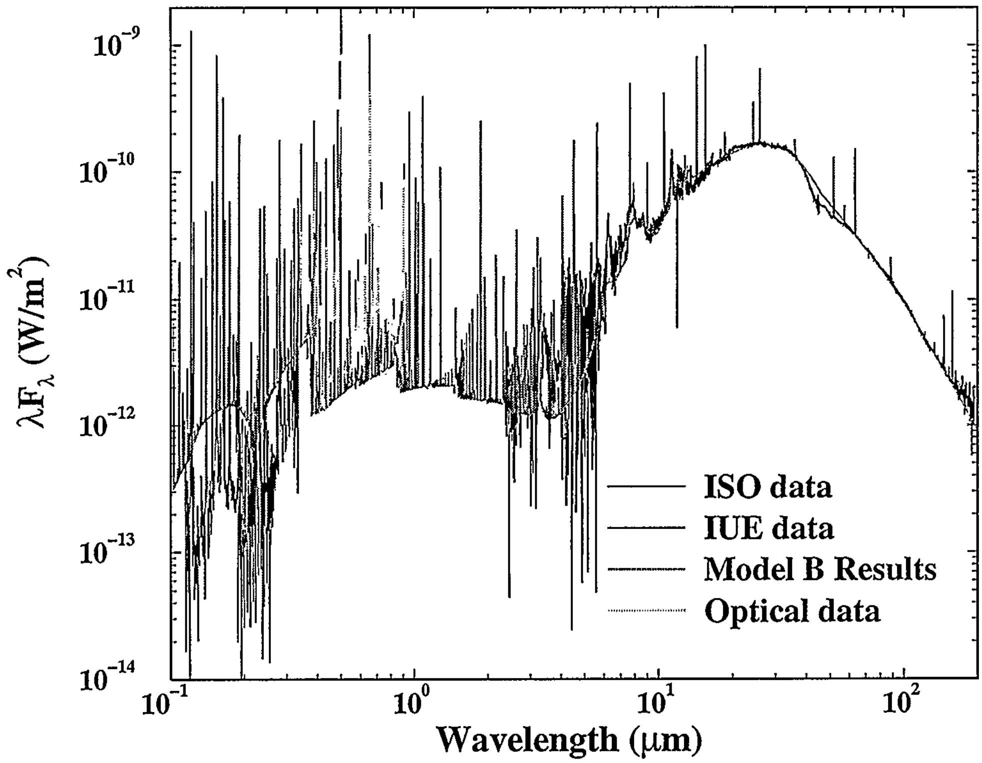

Figure 5.6: NGC 7027 Model B results. 0.075 μm AmC grains with features at 21, 27 amd 33 μm are included in the ionized region. 1.0 μm AmC grain with the same features in the neutral region.

is no obvious wing developing at the longer wavelength side of the feature. The discrepancy seen in the NGC 7027 model is most likely a result of the model and not a change in the feature profile.

5.3 Analysis

$H\beta$ flux is observed at $(1.83 \pm 0.04) \times 10^{-12}$ W/m^2 and the model produces a value of 1.75×10^{-12} W/m^2. This is within 5% of the observations.

Stellar V magnitude is 13.130 which is an adequate fit to the dereddened observed

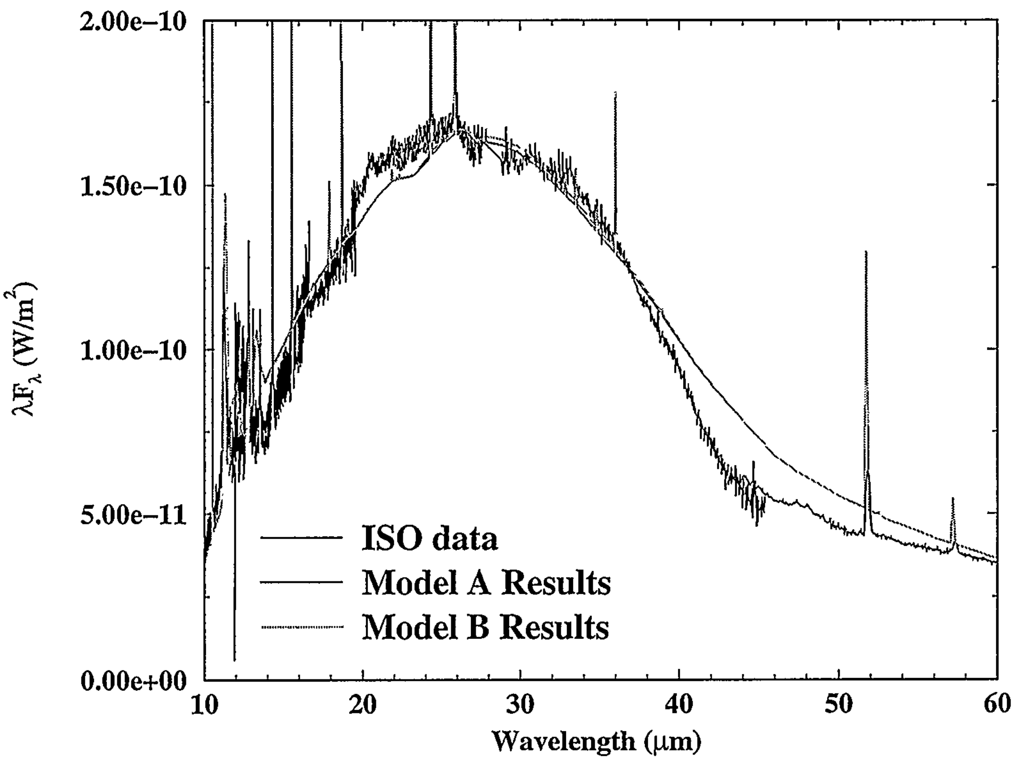

Figure 5.7: NGC 7027 Model A and B peak.

value of 13.30.

The model flux densities in Table 5.2 are not within the error values of the observed values but are largely within 10% of the observed value which is reasonable given the simplified structure of the model nebula.

The dust-to-gas mass ratio for amorphous carbon is derived from the model to be 1.1×10^{-4} in the ionized region. Hoare *et al.* (1992) find a maximum ratio of 7×10^{-4}. Volk & Kwok (1997) derive a value of 9.9×10^{-4}.

The model density of H_2 in the shell in the neutral region is 5.5×10^6 cm^{-3}. This is a reasonable fit with Liu *et al.* (1996) reporting a value a factor of 2 or 3 higher based on CO emission mapping. Volk & Kwok (1997) find the H_2 density at the

	Flux Density (Jy)		
Frequency	Observed	Model	% Difference
1.465 GHz	1.48 ± 0.03	1.39	6%
4.885 GHz	5.66 ± 0.01	6.01	6%
14.965 GHz	6.1 ± 0.1	6.59	8%
149.896 GHz	4.4 ± 0.1	5.19	18%

Table 5.2: Observed and Model Flux Densities for NGC 7027

inner radius of the wind to be 4.9×10^4 cm^{-3} which would also be consistent with this model where there is a factor of 100 difference between the density in the shell and the inner radius of the wind.

From the model optical emission lines, electron density values for the model are 56,100 cm^{-3} and 56,600 cm^{-3} from [NII] and [OIII] lines respectively. The density values are consistent with previous work noted in Section 5.1. The electron temperatures from the model are 22,100 K and 14,500 K from the [OII] and [SII] pairs. The general temperatures derived from observations, including Pottasch(1984) indicate an electron temperature of 14,000 K which is also consistent with our results.

The Zanstra temperatures derived from the model are shown in Table 5.3. The hydrogen and HeII temperatures are consistent with Latter *et al.* (2000) as noted in Section 5.1. HeI temperature is low, which is typical for Zanstra temperatures derived from this line, most likely as a result of coupling between hydrogen and helium (see Section 2.5).

A series of line ratios are presented in Table 5.4. The line ratios, again, serve primarily as a diagnostic tool for finding the electron density and temperature for the model. The model ratios indicate a discrepancy with S and C but an acceptable

	Zanstra Temperatures (K)
Hydrogen	184,000
Helium I	78,800
Helium II	175,800

Table 5.3: Zanstra Temperatures from NGC 7027 Model

fit with O, N, H and He lines.

5.4 Summary

The final model has 0.075 μm AmC dust and PAH grains in the ionized region with no dust features and 1.0 μm AmC dust in the neutral region with 27 and 33 μm features at 0.2 and 0.3 times the continuum. No 21 μm feature is detected. These features are much weaker than what is seen in PPN (which will be discussed in more detail in Chapter 6).

The overall model fit to the ISO data is good, except around 45 μm as a result of the dust modeling. The ISO observations indicate a flatter energy distribution longward of 45 μm which would suggest that there is a feature beginning at 45 μm towards shorter wavelengths. While the right edge of the 33 μm feature is near 45 μm, the increased model flux density compared to the ISO spectrum already exists between 45 and 60 μm. This would suggest that the discrepancy is with the underlying dust component (the amorphous carbon dust) and not the feature. If the underlying continuum of the model is producing higher flux density in that region, the increased flux density shortward of 45 μm could be for the same reason.

We suggest the underlying dust continuum is not as well-fit as in IC 418 largely

Lines	Line Ratios			
	Obs	Model (M90)	Model	
4363/5007	1.87(-2)	1.78(-2)	2.22(-2)	[OIII]/[OIII]
6717/6730	0.46	1.16	0.468	[SII] / [SII]
6584/3727	4.56	4.74	4.31	[NII] / [OII]
1909/5007	0.229	0.282	0.324	CIII] / [OIII]
5755/5007	3.98(-3)	3.28(-3)	4.65(-3)	[NII] / [OIII]
1909	10.26	10.60	4.54	CIII]
3727	0.181	0.218	0.246 *	[OII]
3729	6.69(-2)	8.03(-2)	6.61(-2)**	[OII]
4363	0.259	0.265	0.312	[OIII]
4686	0.494	0.509	0.568	He II
5007	13.9	14.9	14.03	[OIII]
5755	5.52(-2)	4.88(-2)	6.53(-2)**	[NII]
6584	0.82	1.03	1.06**	[NII]
6563	2.78	2.90	2.86	$H\alpha$
6716	1.43(-2)	2.01(-2)	2.76(-2)**	[SII]
6731	3.10(-2)	3.86(-2)	5.90(-2)**	[SII]

Table 5.4: Observed and Model Line Ratios for NGC 7027. Our model values are taken as an equally-weighted average of the three sets of results with * and ** indicating small and large differences, respectively, between those results. Model M90 values are from Middlemass(1990).

as a result of the more complex dust content seen in NGC 7027 and the assumption of spherical symmetry, which is not the case here. The HST image in Figure 5.1 shows a very complicated structure for the nebula which is neither spherical nor symmetric. The set of models made in an attempt to reproduce the nebula better is not sufficient to represent the true physics.

This model is encouraging in that it supports many assumptions about the presence of dust in PN. The overall spectral fit is good. The average dust size in the ionized region is much smaller than in the neutral region which would support the idea of the dust being broken down by the high temperatures of the ionized region. The dust-to-gas mass ratio in the ionized region is smaller, but the H_2 density in the high density shell and the wind region is consistent with previous work. However, inconsistencies in the model spectra have been shown and will require a more sophisticated set of computer modeling programs to explore the nebula better.

The model is a success on the larger scale, having fitted the detail of the ISO spectrum and the flux density and line constraints.

Chapter 6

Conclusion

6.1 Summary

Models for IC 418 and NGC 7027 were made for the ionized regions using Cloudy and for the neutral regions by DUSTCD. We present model spectra that are well-fit to the observed ISO data and consistent with $H\beta$ flux and stellar V magnitude observations.

The 21, 27 and 33 μm features as derived by Volk *et al.* (2002) from PPNe were included in the models as our primary focus and the results support their survival through the evolution into the PN stage.

PN	Dust Features			27 μm/33 μm
	21 μm	27 μm	33 μm	
IC 418	0.2	1.05	1.40	0.75
NGC 7027	0.0	0.2	0.3	0.67

Table 6.1: Summary of Model Dust Features

The 27 and 33 μm features are found to coexist in PPNe and our models support the same result in PNe. The feature strength ratio in Column 5 of Table 6.1 show similar values between the two models. The strengths are similar to those found in PPNe by Volk *et al.* (2002) which show the 21 μm feature strength to range from 0.1 to 1.21 and the 27/33 ratio ranging from 0.62 to 0.94.

The feature strengths for IC 418 are similar to the results for PPN 20000+3239 at 0.28/1.06/1.30 (21/27/33 μm). However, noting that the 21 μm feature strength has likely been overestimated by our model (Section 4.2), there is an argument for the decrease in strength as the object evolves. At 0.1 times the continuum, it would already be at the lower end of what is observed in PPNe.

None of the PPNe presented by Volk *et al.* (2002) bear any resemblance to the combination of feature strengths seen in NGC 7027. 07134+1005 showed the closest strengths to NGC 7027 at 27 and 33 μm but it also shows the strongest 21 μm feature among PPNe by far. It is unclear whether the features were never present in NGC 7027 or if they have been destroyed since it entered the PN phase.

The feature profiles appear to be consistent with those found in PPN. Inconsistencies in the fit in both IC 418 and NGC 7027 are more likely a result of observational data uncertainties or computer modeling assumptions rather than any real evolution of the feature.

6.2 Discussion

IC 418 and NGC 7027 are very different PNe in terms of structure, morphology and the estimated progenitor mass.

The mass of the ionized region for IC 418 is estimated at 0.1 $M_\odot$ (Pottasch 1984). Our model gives a mass of 0.1 $M_\odot$ for the ionized region. This suggests a low-mass progenitor and a more steady mass-loss throughout the AGB phase. There is a low density neutral region which extends out to 80$''$. Figure 4.1 shows what appear to be the beginnings of outflow jets at the top and bottom of the image but is otherwise well-modeled by simulating a spherically symmetric ionized region with no neutral region. The dust radius is quite small (0.01 μm) compared to the more standard estimates used between 0.1 and 1.0 μm for AGB stars and PPNe. Quantum heating effects are more important for such small grains and will need to be better modeled in order to simulate the grain interactions properly.

NGC 7027, on the other hand has only 0.02 $M_\odot$ (Pottasch (1984)) in the ionized region while Gee *et al.* (1984) and Knapp *et al.* (1982) both suggest over 5 $M_\odot$ is expected in the molecular cloud. Our model gives masses of 0.03 $M_\odot$ and 5 $M_\odot$ respectively. This suggests a large mass for the progenitor object and more complicated winds and mass-loss throughout its lifetime. The nebula is observed to be more complicated including outflow jets visible along the major-axis of the nebula, most significantly from the upper left corner of the ionized region. The final model highlights the limitations of our assumptions of spherical symmetry as the dust emission model contains inconsistencies to the ISO fit between 25 and 60 μm. Future models of the more complex nebulae such as this will require more sophisticated treatment of the structure. To a first approximation, however, the model results are able to reveal a better fit to the observations than previously achieved and the inconsistencies merely highlight the work that still needs to be done to provide a better dust model.

The model spectrum produced for both PN are improvements over previous work. They show good fits to the available data and encouraging indications of the physics that is present in PN and reveal new questions about larger PN characteristics as well as the internal grain physics.

6.3 Future work

More well-observed and well-modeled PNe are needed to have better confirmation of the presence and evolution of the 21, 27 and 33 μm features in the PN stage and of the dust in general.

Since both IC 418 and NGC 7027 are young PN, comparisons of models for older PN will be useful to trace the evolution of these features. Also, younger PN, possibly objects closer to the transition between PPN and PN need to be observed and modeled. We would like to explore the evolution of these objects in terms of their precursor objects and in terms of the later morphology of PN both of which have been observed to be incredibly different, as we have shown with these models. It is important to establish how these objects are linked from phase to phase, much as the HR diagram is able to describe the evolution of stars.

The chemistry of the progenitor and in the nebular mass are important in determining the carriers of the three features. The results from better models and observations will be able to determine the environment that most favours these features. Continued laboratory studies into complex molecular structures which can give rise to these features are also encouraged to describe the possible or most likely carrier particles. The combination of these studies gives clues to the nebular environment which can create these particles. This will include dependencies on chemical abundance, temperature distributions and density variations within the nebulae.

While the features presented are observed in extreme carbon-rich environments, it will be useful to include extensive studies on oxygen-rich objects as well. The chemical makeup may be different but the physics will be the same. The evolution of O-rich PN will certainly shed light on the grain physics subject to a different set of initial parameters which may highlight processes predicted in a C-rich environment.

By studying a larger number of objects at different evolutionary stages and with varied nebular characteristics, the results can reveal what and how parameters are important to PN evolution. The mass and temperature of the central star determine, in part, the environment responsible for the current observed nebulae and the physics going on within. The shape, structure and chemistry of the nebulae as a result of mass-loss processes in the AGB phase also define the the conditions which create and surround the dust grains. In turn, the dust physics can be better predicted when the surrounding environment can be better modeled. We want to understand the importance of these nebular parameters to the resulting dust parameters.

Computer modeling of nebular physics will need to be improved to better simulate the more complex nebula being observed.

2-dimensional and 3-dimensional models will increase our ability to describe PN physics especially in complex systems like those seen in NGC 7027 which have non-spherical and non-symmetrical properties. Material is subject to temperature, velocity, and density gradients as a function of position in the nebula. There are also the complicated jet processes which are present in more evolved PN. These will be important processes to model if we are to study objects which are even less spherical than NGC 7027. In order to better describe the complex processes we wish to explore as discussed above, we need to be able to create more realistic models with which to compare those results. As a first step towards more realistic models, it will be important to be able to model non-spherical geometries to see what effect asymmetry will have on the model spectrum.

The physics of smaller grains should also be improved (in Cloudy) in light of the smaller grains which are predicted by the IC 418 model. Improvement with respect to the interaction of the grains with the surrounding nebula would require a better understanding of the dust grain interaction properties (such as the approximation for the probability of electron sticking to the grain and the process of grain charging). Surface effects and quantum heating must be more explicitly modeled in order to accurately model PN.

It is of interest to know what properties can be successfully modeled under the simpler set of assumptions and which dust properties will be critical in modeling nebular physics.

Dust particles, individually and in bulk, must be better described.

Dust properties are currently generalized and simplified since the true particles are complex and more random and variable than can often be simulated in the laboratory. Assumptions of uniformity of size, distribution, shape and atomic content are reasonable for the first approximation of such complicated systems. For instance, we include dust with a single radius whose size represented some average size across the region although the dust changes size between the ionized and neutral regions. We assume spherical grains when this is highly improbable for true grains subject to harsh and non-uniform nebular conditions. Better analysis of dust characteristics and interactions of dust with the nebular environment will require some way to reproduce, among other things, the random sizes and shapes of dust and, as a result, the various associated rotational and vibrational modes available to the grain.

Continued study of the 11.3 μm feature.

As discussed in the IC 418 model, the SiC feature was not able to reasonably fit the 11.3 μm feature observed in the nebula. Inspection of the feature extracted from the comparison of the observations with the model reveals a profile that is not consistent with those presented by Borghesi *et al.* (1985). They do report that the shape and peak of the feature are "significantly driven by size effects". While the Mie theory undoubtedly provides an overly ideal grain model, the complexity of an accurate model has made it difficult to provide a better or more reliable solution. An extensive study of the feature from PN observations, such as undertaken for the 21, 27 and 33 μm feature by Volk *et al.* (2002), may shed more light on the profile in conjunction with laboratory research being conducted.

Appendix A

A.1 Notation

Several sets of notation need to be introduced as being the standards in astronomy.

A.1.1 Ionization

Ionization is noted with roman numerals following the atomic symbol for a species with roman numeral I referring to the ground state. For example, neutral hydrogen is HI. OII and OIII refer to the singly and doubly ionized oxygen atoms respectively.

A.1.2 Forbidden and Semi-forbidden Lines

Notation for line emission is specified with square brackets: [ ]. Forbidden lines are indicated with a pair of square brackets such as [OIII], a line emission from doubly-ionized oxygen. Intercombination lines or "semi-forbidden" lines are indicated by a single square bracket following the atomic species: CIII]. These transitions follow LS coupling rules except $\Delta S \neq 0$. Permitted line emissions do not have any brackets around them.

A.1.3 Line Series

Energy level transitions have also been given names which will be used in discussion throughout the thesis. The name of each transition refers to the lower level of an absorption or emission transition. Lyman transitions refer to transitions with lower level n=1. Balmer refers to transitions to n=2, Paschen to n=3, Brackett to n=4, etc.

Each line can be more specifically identified by a greek letter that identifies the level separation involved in the transition. α refers to $\Delta n = 1$. β refers to transitions where $\Delta n = 2$. Lyman α (or $Ly\alpha$), for instance, refers to transitions between n=2 to n=1.

In astronomy, we refer specifically to the line emissions from the hydrogen atom. For example, Lyman α lines are specifically transitions into or out of level n=1 within the hydrogen atom. A special case for notation is for Balmer lines from the hydrogen atom. These are very important lines in observations which are noted with a upper case letter 'H': $H\alpha$, $H\beta$ and so forth.

The specific frequency for each transition is given by

$$\frac{1}{\lambda_{i,j}} = R_1 \left(\frac{1}{n_j^2} - \frac{1}{n_i^2} \right) \tag{A.1}$$

where R_1 is the hydrogen Rydberg constant, c the speed of light, j is the quantum number of the lower level and i the quantum number of the upper level of the transition. $n_j = 2$ for the Balmer series.

Then the actual wavelengths for each hydrogen line can be calculated.

Table A.1: Wavelengths for Selected H Line Emissions

Line	Lyα	$H\alpha$	$H\beta$
Wavelength (Å)	1216	6563	4861

The *continuum* for a transition (e.g. Lyman continuum) refers to the portion of the bound-free continuum that is produced with energies greater than the transition *jump*. The *jump* refers to the wavelength where an electron sitting at the associated energy level escapes from the atom. For example, the Lyman jump is the wavelength at which an electron in the ground state (n=1) gains exactly enough energy to escape from the atom.

A.1.4 Photometric Bands

The electromagnetic spectrum is divided into several photometric bands. Each band is assigned a letter as an index and a central wavelength which is shown in Table A.2.

Table A.2: The Central Wavelengths of Photometric Bands

Filter	U	B	V	R	I	J	H	K	L	M	N
λ (μm)	0.36	0.44	0.55	0.70	0.90	1.25	1.65	2.20	3.40	5.00	10.20

U is ultraviolet. B is blue. V is visible. R is red. I is infrared.

A.2 Units

A.2.1 Energy: The Rydberg

The unit for energy used by Cloudy is the Rydberg which is defined by one of two wave numbers, $R_\imath$.

$$1 \text{ Rydberg} = chR_\imath$$

where $R_\imath$ can be either the hydrogen R, R_H, or the infinite mass R, R_∞. R_H is defined by the ionization potential of hydrogen

$$R_H = 109677.576 \text{ cm}^{-1}.$$

This is the value used by Cloudy prior to 1988. Current versions use the infinite mass wave number, R_∞, which is defined as

$$R_\infty = \frac{2\pi^2 m_e q_E^4}{ch^3} = 109737.315 \text{ cm}^{-1}.$$

In terms of energy,

$$1Ryd = chR_\infty = 2.179874 \times 10^{-11}\text{erg} = 13.6057\text{eV}. \tag{A.2}$$

A.3 Dust-to-gas Mass Ratio

The nominal dust-to-gas mass ratio is 298.44 : 1 for carbon-based dust grains such as graphite and amorphous carbon.

We first assume that one solar abundance of carbon is converted into dust grains.

$$\frac{C}{H} = 3.63 \times 10^{-4} \text{ or } \frac{H}{C} = 2754.82.$$

We assume that in the gas there are 9 H atoms for 1 He atom resulting in the mass per hydrogen atom of the gas to be 1.3 AMU/H atom. This gives us a mass per carbon atom of the gas:

$$m_g = \frac{H}{C} \times 1.3\ AMU/H = 2754.82\ H/C \times 1.3\ AMU/H = 3581.266\ AMU/C$$

Using a carbon mass of 12 AMU, the nominal gas-to-dust ratio is given as

$$\frac{m_g}{m_d} = 3581.266\ AMU/12\ AMU = 298.44.$$

The nominal ratio requires a small correction between the code calculating dust properties and Cloudy. The correction depends on the dust opacity files created for input to Cloudy and number of H atoms per grain.

$$\text{Hatoms/grain} = H/C \times \text{Catoms/grain} \tag{A.3}$$

The number of carbon atoms per grain is found by taking the mass ratio

$$\frac{Catoms}{grain} = \frac{m_{grain}}{m_{carbon}}$$

where $m_{grain} = \frac{4}{3}\pi a^3 \rho_{grain}$ and $m_{carbon} = 12\ AMU$. Density for the amorphous carbon grain is taken to be 1.81 g/cm^3 as per Rouleau and Martin (1991) derived for a BE1 grain.

The input files contain the value for opacity as $\eta_1 = \pi a^2 Q$ and $\eta_2 = 4\pi a^2 Qv/\text{Hatom}$. The correction to the nominal dust-to-gas ratio is found by using Equation A.3 and taking the ratio of η values.

$$\text{corrected nominal value } = \eta_2 \, \frac{\text{Hatoms/grain}}{4 \times \eta_1}.$$

So, the gas-to-dust mass ratio is found by

$$A \times \frac{\text{corrected nominal value}}{\text{nominal value}}$$

where A is the abundance value set as input to Cloudy.

For IC 418, the dust abundance is set to 0.48 times the nominal value for a 0.01 μm AMC grain which gives a dust-to-gas mass ratio of 1.6×10^{-3} in the ionized region.

For NGC 7027, the dust abundance is set to 0.032 times the nominal value for a 0.075 μm AMC grain which gives a dust-to-gas mass ratio of 1.1×10^{-4} in the ionized region.

Bibliography

Acker, A., et al, 1992, Strasbourg-ESO Catalogue of Galactic Planetary Nebulae (Garching bei München, European Southern Observatory

Aller, L.H., 1984, Physics of Thermal Gaseous Nebulae: Physical Processes in Gaseous Nebulae, (Dordrecht, Holland: D. Reidel Publishing Company)

Barlow, M.J., 1987, MNRAS 227, 161

Borghesi, A., E. Bussoletti, L. Colangeli, C. De Blasi, 1985, AA 153, 1

Bujarrabal, V., A. Fuente, and A. Omont, 1994, ApJ 421, L47

Bregman, J.D., L.J. Allamandola, A.G.G.M. Tielens, T.R. Geballe, and F.C. Witteborn, 1989, ApJ 344, 791

Cahn, J.H., and J.B. Kaler, 1971, ApJS 22, 319

Ciardullo, R., et al, 1999, ApJ 118, 488

Clegg, P.E., 1999, in The Universe as Seen by ISO (Vol 1), ed. P. Cox and M.F. Kessler (ESA Publications Division, ESTEC, Noordwijk, The Netherlands), 39

Cohen, M, and M.J. Barlow, 1974, ApJ 193, 401

Cohen, M., et al, 1975, Apj 196, 179

de Graauw, T., 1999, in The Universe as Seen by ISO (Vol 1), ed. P. Cox and M.F. Kessler (ESA Publications Division, ESTEC, Noordwijk, The Netherlands), 31

Draine, B.T. and Hyung Mok Lee, 1984, ApJ 285, 89

Ferland, G. J., 2001, Hazy, a brief introduction to Cloudy 94

Frenklach, M., C.S. Carmer, and E.D Feigelson, 1989, Nature 339, 196

Furton, D.G., and A.N. Witt, 1992, ApJ 386, 587

Gee, G., J.P. Emerson, P.A.R. Ade, E.I. Robson and I.G. Nolt, 1984, MNRAS 208, 517

Gesicki, K., A. Acker and R. Szczerba, 1996, AA 309, 907

Gleizes, A. Acker, and B. Stenholm, 1989, AA 222, 237

Goebel, J.H., and S.H, Moseley, 1984, ApJ 290, L35

Guillois, O., I. Nenner, R. Papoular, and C. Reynaud, 1996, ApJ 464, 810

Henry, R.B.C., L.B. Kwitter and J.A. Bates, 2000, ApJ 531, 928

Hoare, M.G., 1990, MNRAS 244, 193

Hoare, M.G., P.F. Roche and R.E.S. Clegg, 1992, MNRAS 258, 257

Hora, J.L., L.K. Deutsch, W.F. Hoffmann, G.G. Fazio, and K. Shivanandan, 1993, ApJ 413, 304

Hyung, S. and L.H. Aller, 1994, PASP 106, 145

Jäger, C., et al, 1998, AA 339, 904

Jaminet, P.A., et al, 1991, ApJ 380, 461

Knapp, G.R., et al, 1982, ApJ 252, 616

Kwok, S., C.R. Purton and P.M. Fitzgerald, 1978, ApJ 219, L125

Kwok, S., 1980, ApJ 236, 592

Kwok, S., K. Volk, and B.J. Hrivnak, 1989, ApJ 345, L51

Kwok, S., 2000, The Origin and Evolution of Planetary Nebulae, (Cambridge: Cambridge University Press)

Kwok, S., 2001, Physics and Chemistry of Interstellar Medium, unpublished notes, University of Calgary

Latter, W.B., et al, 2000. ApJ 539, 783

Leung, C.M., 1976, ApJ 209, 75

Liu, X.-W., et al, 1996, AA 315, L257

Louise, R., A. Macron, C. Pascoli, and E. Maurice, 1987, AAS 70, 201

Masson, C.R., 1989, ApJ 336, 294

Masson, C.R., 1986, ApJ 302, L27

Mendez, R.H., R.P. Kudritzki, A. Herrero, D. Husfeld, and H.G. Groth, 1988, AA 190, 113

Middlemass, D., 1990, MNRAS 255, 294

Meixner, M., C.J. Skinner, E. Keto, A. Zijlstra, M.G. Hoare, J.F. Arens, and J.G. Jernigan, 1996, AA 313, 234

Monk, D.J., M.J. Barlow, and R.E.S. Clegg, 1990, MNRAS 242, 457

Papoular, R., 2000, AA 362, L9

Phillips, J.P., A. Riera, and A. Mampaso, 1990, AA 234, 454

Pottasch, S.R., W.M. Goss, E.M. Arnal and R. Gathier, 1982, AA 106, 229

Pottasch, S.R., 1984, Planetary Nebula: A Study of Late Stages of Stellar Evolution, (Dordrecht, Holland: D. Reidel Publishing Company)

Pottasch, S.R., B. Baud, D. Beintema, J. Emerson, H.J. Habing, S. Harris, J. Houck, R. Jennings, and P. Marsden, 1984, AA 138, 10

Rieke, G.H., and M.J. Lebofsky, 1985, ApJ 288, 618

Roelfsema, P.R., W.M. Goss, S.R. Pottasch and A. Zijlstra, 1991, ApJ 251, 611

Rouleau, F., and P.G. Martin, 1991, ApJ 377, 526

Salas, J.B., S.R. Pottasch, D.A. Beintema, and P.R. Wesselius, 2001, AA 367, 949

Schutte, W.A., A.G.G.M. Tielens, and L.J. Allamandola, 1993, ApJ 415, 397

Su, K., 2000, PhD Thesis, University of Calgary

Taylor, A.R. and S.R. Pottasch, 1987, AA 176, L5

Taylor, A.R., G.T. Gussie, and W.M. Goss, 1989, ApJ 340, 932

Volk, K., and M. Cohen, 1990, ApJ 100, 485

Volk, K., and S. Kwok, 1997, ApJ 477, 722

Volk, K., S. Kwok, and B.J. Hrivnak, 1999, ApJ 516, L99

Volk, K., 2000, Notes on Interstellar Medium for Asph 503, unpublished notes, University of Calgary

Volk, K., 2000, Notes on Forbidden Lines, unpublished notes, University of Calgary

Volk, K., S. Kwok, B.J. Hrivnak and R. Szczerba, 2002, ApJ 567, 412

Walker, G., 1987, Astronomical Observations: An Optical Perspective, (Cambridge: Cambridge University Press)

Willner, S.P., B. Jones, R.C. Puetter, R.W. Russell and B.T. Soifer, 1979, ApJ 234, 496

Yan, M., S.R. Federman, A. Dalgarno, and J.E. Bjorkman, 1999, ApJ 515, 640

Zhang, C.Y., and S. Kwok, 1992, ApJ 385, 255